Spring 2024

# Differences in the metabolic outputs of *Caulobacter crescentus* modify the kinetics of silver nanoparticle dissolution

Tyler M. Hicks , '24

# Differences in the metabolic outputs of *Caulobacter crescentus* modify the kinetics of silver nanoparticle dissolution

Presented as a Senior Course Thesis in Chemistry

Tyler M. Hicks

May 2024

Swarthmore College

Advisor: Kathryn R. Riley

## Table of Contents

## List of Common Abbreviations

AgNP – silver nanoparticle

AMP – adenosine monophosphate

AuNP – gold nanoparticle

BCA – bicinchoninic acid

BSA – bovine serum albumin

CE – capillary electrophoresis

c-di-GMP – cyclic diguanylate monophosphate

DLS – dynamic light scattering

ENM – engineered nanomaterial

GSH – glutathione

LC-MS – liquid chromatography-mass spectrometry

LSSV – linear sweep stripping voltammetry

NOM – natural organic matter

$OD_{600}$ – optical density at 600 nm

PDI – polydispersity index

PYE – peptone yeast extract

ROS – reactive oxygen species

SAM – S-adenosylmethionine

SM – spent medium

$\zeta$ – zeta potential

## List of Figures and Tables

## Abstract

Silver nanoparticles (AgNPs) are widely used within commercial products due to their distinct antibacterial and antimicrobial properties. As their utilization continues to increase, their inevitable improper disposal could present lasting environmental ramifications due to their non-specific biotoxicity. One microorganism of interest is *Caulobacter crescentus*, a common freshwater bacterium found in locations where AgNPs end after their disposal. *C. crescentus* has two distinct cell types—a stalked and a swarmer form—each with their own unique function and metabolic outputs. Approximately 15% of the *C. crescentus* metabolome varies with cell cycle, thus making this an interesting and environmentally relevant model organism for this work. Adsorbates, like proteins and other metabolites readily adsorb to the surface of AgNPs forming eco-coronas, which can alter the biological fate of AgNPs. A process of synchronizing the bacteria to the same cell-cycle interval was accomplished and complex mixtures of excreted matter from the *C. crescentus* were isolated at different intervals in the cell cycle. These mixtures were then used to create *C. crescentus* eco-coronas. Electrochemical techniques such as linear sweep stripping voltammetry (LSSV) in combination with dynamic light scattering (DLS) were used to evaluate the impact of *C. crescentus* eco-coronas on AgNP size, charge, and dissolution. Later stages in the *C. crescentus* cell-cycle were shown to contain more complex mixtures of adsorbates and lead to higher AgNP dissolution rates, thus demonstrating the utility of *C. crescentus* to model the complex environmental reactivity of AgNPs.

# Chapter 1: Introduction

The utilization of engineered nanomaterials (ENMs) in many sectors of life, including industry, energy technologies, medicine, and commerce, has greatly increased in the last decade due to their unique, tunable properties. Silver nanoparticles (AgNPs), in particular, have received increased attention due to their antibacterial and antimicrobial properties.[1–3] As AgNPs are used in much higher quantities than in prior years, we must not only investigate their beneficial impact to human health, but also their potential detrimental impact on the environment due to their inevitable release during production, use, and disposal. The mechanisms by which AgNPs exhibit antibacterial and antimicrobial characteristics is not entirely understood, however, it is thought to be correlated to the dissolution of the AgNPs into silver ions.[4] Dissolution is merely one environmental transformation that AgNPs can undergo. However, dissolution has important implications regarding the form of Ag in the environment (nanoparticulate or ionic) and the potential toxicity of AgNPs to environmental organisms.[5–8]

AgNPs are often discarded into landfills or they enter the water column after passage through wastewater treatment plants.[9] These environments are rich with biological and organic species leading to the formation of what is termed an eco-corona. Adsorbates, like proteins, natural organic matter (NOM), and inorganic ions readily adsorb to the surface of AgNPs forming eco-coronas, which can alter the biological fate of AgNPs.[10–12] Thus, it is important to understand the complex chemistries that control AgNP reactivity at the nano-bio interface using environmentally relevant models. One such model system is *Caulobacter crescentus*, a bacterium that is often present in the same areas where AgNPs are inevitably discarded.[9,13] Therefore, this work seeks to use *C. crescentus* as a model system from which to derive relevant, complex eco-coronas in order to investigate the impact of eco-coronas on AgNP dissolution as a

stepping stone towards understanding the environmental transformation of AgNPs. To this end, a suite of analytical electrochemical and spectroscopic techniques was used to analyze the intricacies of the modifications of AgNP dissolution kinetics as a result of the formation of complex *C. crescentus* eco-coronas.

### 1.1: Engineered nanomaterials and their environmental fate

An ENM is any material that has been manufactured to have one dimension of 100 nm or less. There has been a significant increase in the applications of ENMs, ranging from incorporation into commercial products to employment in nanomedicines. For example, inorganic nanoparticles such as zinc oxide (ZnO) and titanium dioxide ($TiO_2$) are used as UV filters in mineral sunscreens due to their near colorless appearance when applied to skin.[14] The nanomedicine market, which was valued at approximately 293 billion USD in 2022, is expected to grow to approximately 351 billion USD by 2025.[15] ENMs are rapidly becoming an integral part of the chemical market due to their unique tunable properties based on their controllable size and surface chemistry. Particular to this work, AgNPs have been widely used in a plethora of different applications due to their antibacterial and antimicrobial properties.[2,4]

The tunability of the antibacterial and antimicrobial characteristics of AgNPs make them vastly beneficial for maintaining and improving the quality of life of humans in today's globalized world. These applications include the process of recycling wastewater to remove harmful microbes,[1] preserving commercial products like makeup and skincare,[3] and impregnation into fabrics to kill harmful bacteria.[16,17] It is important to note that the mechanism of AgNP toxicity for bacteria and microorganisms is nonspecific and cannot distinguish between harmful bacteria and beneficial bacteria. To that extent, it is important to study the way in which AgNPs, and ENMs more broadly, interact with the ecosystems in which they will end up.

AgNPs are produced in massive quantities; some figures estimate that more than 600 metric tons of AgNPs are produced each year![18] In their various applications, these materials will eventually be discarded through intentional disposal or through unintentional release like washing a material which has been imbedded with AgNPs. This can be problematic as there is a high likelihood that AgNPs will accumulate in improper locations. For instance, if someone washes a pair of socks which have been impregnated with AgNPs, there is a good chance that some of these AgNPs will enter wastewater treatment plants and even freshwater sources like lakes and streams.[19,20] Once the AgNPs are present in these environmentally critical zones, many different physicochemical transformations can occur, including but not limited to aggregation, agglomeration, redox chemistries, and adsorption of biomolecules onto their surface.[5]

Aggregation of nanomaterials is affected by a wide variety of factors related to both the medium in which they are suspended (pH, ionic composition, ionic strength, etc) as well as the materials themselves (size, surface coating, etc).[8] The mechanism by which aggregation occurs is defined using Derjaguin-Landau-Verwey-Overbeek (DLVO) theory which explains how the stability of a colloid is affected by its presence in aqueous medium. DLVO theory combines the attractive forces of traditional Van der Waals forces with repulsive, electrostatic forces to describe the likelihood for two particles to interact.[21,22] DLVO theory can model aggregation in systems with ENMs due to their nanoscale size. AgNPs are typically electrostatically stabilized via a coating with a charged molecule like citrate to limit homoaggregation (aggregation of one particle to another particle of the same kind).[6,8,23] However, if the solution in which the AgNPs are suspended has sufficient ionic strength, the cations can induce homoaggregation by compressing the electric double layer thus reducing the repulsive forces between two particles. It is important to note that DLVO theory does not explain all the ways in which aggregation can

occur; key to this work, aggregation can be induced by the presence of bio- and organic molecules.

The most widely accepted mechanism for bacterial toxicity via AgNPs is the dissolution of AgNPs into ionic silver. Thus, understanding the mechanism by which dissolution of AgNPs occurs is pivotal. Oxidative dissolution, the major dissolution mechanism of AgNPs, occurs when silver atoms at the surface of a AgNP encounter an oxidizing species such as diatomic oxygen. Under appropriate conditions, the surface Ag atoms can be oxidized to Ag(I) according to:

$$4Ag_{(s)} + O_{2(aq)} + 4H^{+}_{(aq)} \rightarrow 4Ag(I)_{(aq)} + 2H_2O_{(l)} \quad (1)$$

Some of the factors which influence dissolution include the solution pH, ionic composition and strength of the solution, the size and surface coating of the particle, and the presence of adsorbates in solution.[2,8,24–27] Particular to this work, the distinction between the dissolution rate of different particle sizes is of utmost importance; the smaller a particle is, the faster the particle will dissolve due to the increased surface area to volume ratio.[24,28,29]

Upon oxidative dissolution of AgNPs the degradation of several biochemical pathways begins. Organic and biological materials have a high affinity for Ag(I) which explains the ways in which ionic silver readily and rapidly disrupts cellular membranes,[30] critical enzymes,[31] and RNA.[26,30,31] Additionally, AgNPs can increase concentrations of reactive oxygen species (ROS) at a cellular level,[31] which leads to RNA and DNA modifications that disrupt cellular reproduction.[7,7,32,33] It has been further demonstrated that ROS are produced at a much higher level in the presence of smaller particles as opposed to larger particles due to their increased surface area to volume ratio.[34]

### 1.2: Eco-coronas and their modulation of nanoparticle reactivity

When a AgNP comes into contact with environmentally or biologically relevant media rich in NOM and biomolecules (e.g., proteins, carbohydrates, metabolites, lipids, etc.), the adsorbates can exchange with or overcoat the stabilizing ligands on the AgNP surface to form an eco-corona.[10,35] Physical adsorption of large biomolecules such as proteins or metabolites to the surface of a AgNP can increase the effective particle size and cause some level of aggregation through Debye screening, or an effective decrease in the charge of the AgNP due to adsorbed molecules with different charges.[36,37] Corona formation can lead to decreased aggregation through steric stabilization of the AgNP or it can lead to increased aggregation or dissolution through elimination of electrostatic stabilization. Likewise, corona formation can lead to decreased dissolution by limiting oxygen accessibility to and Ag(I) diffusion from the AgNP surface or it can lead to increased dissolution through a nucleophilic dissolution mechanism **(Figure 1)**.[24,28,30]

Eco-corona formation is dynamic. Initially, adsorbates which are highest in concentration will adsorb first, however, this initial corona formation is not long lived and as time passes, adsorbates that have a higher affinity for the NP's surface will replace the initial corona constituents. This chemical phenomenon is known as the Vroman Effect.[38,39] The layer of high affinity adsorbates which are directly bonded to the nanoparticle surface form what is called the hard corona.[10,11] The remaining adsorbates in the bulk solution can form the so-called soft corona, which is a secondary layer of adsorbates with low affinities for the nanoparticle surface itself. Thus, the interactions which facilitate the formation of the soft corona are adsorbate-adsorbate interactions.[10–12,35,37] An interesting effect of this two-layer eco-corona is the frequent changes in the properties of a particular nanoparticle-eco-corona complex. For example, due to

the low affinity interactions of adsorbates in the soft corona, the corona can be entirely reconstructed via desorption and adsorption events as the NP-corona complex enters different environmental compartments.[40,41]

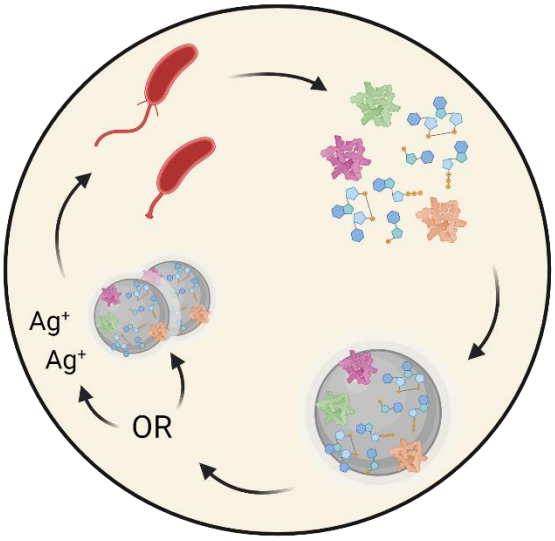


**Figure 1. Schematic of the interaction of a AgNP with *C. crescentus* excreted biomolecules.** *C. crescentus* in both its stalked and swarmer cell type excrete a mixture of various biomolecules, which can adsorb to the surface of a pristine AgNP forming an eco-corona. The *C. crescentus* eco-corona modulates the reactivity of AgNPs by enhancing various transformations including dissolution and aggregation.

Eco-coronas can not only alter AgNP aggregation and dissolution behaviors, but can also modulate the way in which AgNPs are recognized by living organisms. Results are not entirely conclusive as to the impact of eco-coronas on the biological toxicity of AgNPs, with varying reports that the formation of eco-coronas on AgNPs have both reduced and increased the bactericidal properties of the AgNPs.[42–44] Research suggests that this conflicting behavior is the result of the composition of the eco-corona itself. For instance, AgNPs with an eco-corona of NOM have decreased toxicity while those composed of proteins have increased toxicity.[40,42,44] This suggests that the mechanism by which AgNP cytotoxicity is modulated via eco-corona

formation is related to the way in which a cell recognizes the coating of the particle as opposed to the particle itself.

### 1.3: *C. crescentus* as an environmental model system

Many previous studies on the impacts of eco-coronas focus on a single adsorbate (one protein, biomolecule, or organic macromolecule). However, it is pivotal to explore the formation of complex eco-coronas by way of environmentally relevant mixtures of adsorbates. One strain of bacteria that can be used to generate complex eco-coronas is *C. crescentus*. An oligotrophic alphaproteobacterium, *C. crescentus* is often found in nutrient deficient environments which are often composed of large amounts of wastewater (e.g., wastewater treatment plants, sewage systems, etc).[9] This is important because it is these same environments where AgNPs are improperly discarded or end up after rounds of washing.[1,32]

*C. crescentus* is a unique bacterium due to its dimorphic life cycle (**Figure 2**).[45] At the start of the cell cycle, the bacteria are in a swarmer phase which is distinguished by a flagellum - a threadlike structure which facilitates the rapid movement of cells through aqueous media.[46] The swarmer cell then sheds its flagellum which transforms it into a predivisional cell.[47] Next, a stalk, or prostheca, and a holdfast form and the cell is in a stalked phase. The holdfast produces an adhesive compound which facilitates the sticking of a *C. crescentus* cell to a surface.[48] While swarmer cells search for sources of nutrients in its environment, the adhesion of stalked cells to surfaces facilitates the formation of a biofilm, a structured bacterial community which enables the efficient spreading of nutrients among the stationary cells.[49,50] It is the formation of a stalk and holdfast that initiates DNA replication and the general process of asymmetric cellular division.[51] The stalked cell type serves as the basis for the cellular division which produces a

genetically identical swarmer cell which can then begin the process of cellular development once again.[52]

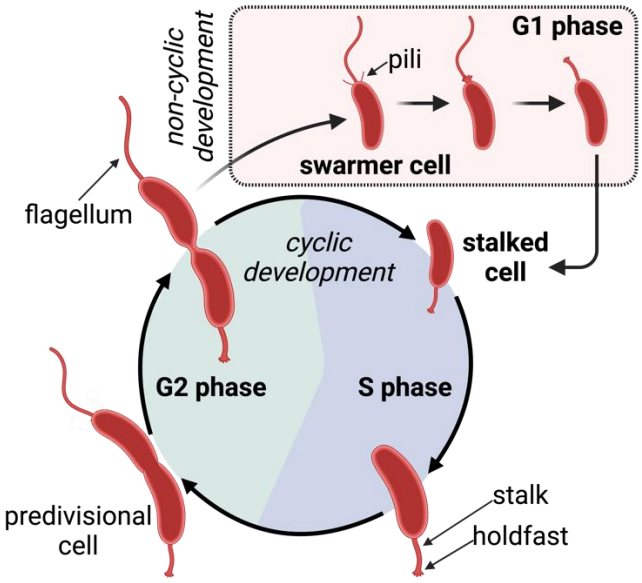


**Figure 2. Schematic showing the cell cycle of *C. crescentus***, which is distinguished by its dimorphic life cycle including a stalked and swarmer cell type.

Another extremely important facet of *C. crescentus* is the variance of its metabolome as a function of cell cycle stage. Previous research has shown that approximately 14% of the *C. crescentus* metabolome varies with the cell cycle.[53] The majority of the metabolites that vary are sulfur based which is of importance due to the process of sulfur assimilation (the conversion of inorganic forms of sulfur to bioavailable sulfur metabolites).[54] Sulfur assimilation is needed for the transformation of the initial swarmer cell to a stalked cell during the transition between the G1 and S cell phases.[55] In a synchronized culture of *C. crescentus* where all cells are at the same developmental stage, there is a surge in the concentration of sulfur metabolites during later stages of growth after the cells have divided. Some of the sulfur metabolites of interest to this

work and more generally related to *C. crescentus* metabolism are glutathione (GSH) and its precursor intermediates (cysteine, γ-glutamylcysteine), as well as S-adenosylmethionine (SAM) and its precursor intermediates (methionine and homocysteine).[54,56] GSH is a critical metabolite which has been directly linked to proper cellular growth in various populations of *C. crescentus*, while SAM is critical for mediating methylation reactions as well as for producing key signaling molecules like autoinducer-2.[53,57]

Another metabolite of interest is the bacterial messenger molecule cyclic di-GMP (c-di-GMP). The concentration of C-di-GMP has been shown to peak a short time after the conversion of a swarmer cell to a stalked cell, similar to the sulfur metabolites described above.[58,59] Moreover, the concentrations of c-di-GMP in synchronized cultures are approximately 3 times that in unsynchronized cultures.[53] This fact, alongside its pivotal nature in determining when the aforementioned G1 to S transition occurs[60], make c-di-GMP an interesting metabolite to study in relation to the *C. crescentus* cell cycle. Although all the aforementioned metabolites are of critical importance for cellular growth, this work will primarily build upon prior research in the Riley Group which has linked GSH to changes in AgNP dissolution while also seeking to corroborate results with other changes in key metabolites.

Although *C. crescentus* has unique properties, it has broad implications. *C. crescentus* is one of many alphaproteobacteria in the *Hyphomonadaceae* bacterial family that inhabit similar environments where AgNPs are likely to be discarded. Many species in this family, such as the *Hyphomonas neptunium* and the *Hirschia baltica*, also exist in both a stalked and swarmer cell type.[61,62] Additionally, many of these bacterial species produce many of the same metabolites that have been discussed above in similar concentrations as *C. crescentus*.[63] Therefore, using the metabolites that *C. crescentus* produces to explore how AgNP dissolution kinetics is affected by

the development of eco-coronas, allows for broader conclusions to be drawn in relation to the environmental reactivity of AgNPs.

### 1.4: Research aims

To date, most eco-corona research has focused on either the formation of a simplified eco-corona (one biomolecule of interest) or *in situ* work (investigating the composition of eco-coronas formed in mesocosms). However, little work has been done between these extremes to bridge our understanding of corona formation at different scales, and there is a need for additional studies that investigate complex coronas (formed from 2 or more adsorbates) and *in vivo* coronas (formed from biological organisms). Through investigation of the latter, this work aims to contribute to predicting the fates of ENMs, designing ENMs for proper and safe environmental impact, and developing ways to control eco-corona compositions.[10,11,35]

Previous work in the Riley Lab has used *C. crescentus* as an environmentally relevant organism from which to derive complex eco-coronas. In this prior work, spent media was isolated from asynchronous cell cultures and AgNP dissolution behaviors were evaluated. In this study conducted with 40 nm citrate stabilized AgNPs, there was no direct correlation observed between cell growth and AgNP dissolution. The goal of this study was to evaluate whether the unique biomolecules excreted by *C. crescentus* in different developmental stages would uniquely modify AgNP dissolution. As a result, a method for cell culture synchronization and subsequent isolation of *C. crescentus* metabolites was developed. In parallel, in this work dissolution studies were performed with 40 nm citrate stabilized AgNPs and 10 nm citrate stabilized AgNPs to expand our understanding of how not only the composition of the eco-corona affects AgNP dissolution, but how that phenomena might be uniquely affected by the particle size.

These eco-coronas and their modulation of environmental reactivity were also compared to available metabolomic data on *C. crescentus* in an attempt to explain the visible trends. This study seeks to better understand the nano-bio interface in ways that have not previously been explored. As opposed to exploring this field at the extremes of *in vitro* studies with singular adsorbates or *in vivo* studies, this study attempts to build a theoretical bridge between the extremes to make further conclusions about the environmental impacts of ENMs as a class of nanomaterials.

# Chapter 2: Materials and Methods

## 2.1: Chemicals

Ammonium chloride (ACS), Bacto™ Peptone, calcium chloride dihydrate (99+%), iron(II) sulfate heptahydrate (98%), magnesium sulfate heptahydrate (99+%), potassium phosphate monobasic (ACS), and yeast extract were purchased from ThermoFisher Scientific (Heysham, England). Bacto™ Agar was purchased from Becton, Dickinson and Company (Sparks, MA). Anhydrous D-(+)-Glucose was purchased from MP Biomedicals (Solon, OH). Percoll™ was purchased from Cytiva Life Sciences (Uppsala, Sweden). Sodium citrate monobasic (≥99.5%), sodium chloride (≥99.5%), sodium hydroxide (99%) and sodium phosphate dibasic (≥99.5%) were purchased from Sigma-Aldrich (St. Louis, MO). BioPure citrate-stabilized AgNPs with a nominal diameter of 10 and 40 nm were purchased from NanoComposix and were provided at a concentration of 1 mg $mL^{-1}$ suspended in a 2 mM sodium citrate solution (La Jolla, CA). All 10 nm AgNPs were taken from lot number SLD0068 and all 40 nm AgNPs were taken from lot number SDC0010. All AgNPs were handled in a dark room to prevent UV-induced transformations such as aggregation and dissolution.

All work was done in a buffer solution containing 15 mM sodium citrate monobasic and 15 mM sodium chloride in Millipore water (18.2 MΩ cm at 25℃). This buffer was prepared at the start of each week and was adjusted to a final pH of 5.2 by dropwise addition of either 1.0 M or 0.1 M sodium hydroxide. This buffer will herein be referred to as the citrate buffer.

## 2.2: Preparing asynchronous cultures of *C. crescentus*

Peptone yeast-extract (PYE) growth medium was prepared according to the following specifications: 0.2% w/v BactoPeptone®, 0.1% w/v yeast extract, 0.5 mM $CaCl_2$, and 1 mM $MgSO_4$ in Millipore water. Agar plates were poured from an agar-enriched PYE medium which

contained 1.5% w/v BactoAgar. Prior to pouring the plates, the agar-enriched PYE medium was autoclaved for 30 minutes and allowed to cool for 2 hours at room temperature. Plates were then poured using sterile technique to a solution height of approximately 1 cm, covered, stored overnight at room temperature, and then stored at 4°C for up to 2 weeks. Fresh agar plates were poured prior to the inoculation of each new bacterial culture.

Glycerol stocks of *C. crescentus* strain NA1000, which were provided by Dr. Michael Laub from the Massachusetts Institute of Technology, were stored at -80°C and used to inoculate fresh agar plates. The frozen glycerol stock was allowed to thaw, whereupon a sterile wooden pick was briefly dipped into the stock and then the plate was streaked. Each plate that was streaked was allowed to grow overnight at room temperature and then incubated at 30°C for two days. Plates which formed visible, discrete colonies were then covered in Parafilm and stored at 4°C and re-plated every week.

### 2.3: Preparing synchronous cultures of *C. crescentus*

As opposed to the nutrient-rich PYE media, the synchronization process requires growth of *C. crescentus* in a nutrient-poor media, M2G media. This media is composed of 0.87 g/L $Na_2HPO_4$, 0.54 g/L $KH_2PO_4$, 0.50 g/L $NH_4Cl$, 0.2% w/v glucose, 0.5 mM $CaCl_2$, 0.5 mM $MgSO_4$, and 0.01 mM $FeSO_4$. M2G media was autoclaved for 30 minutes and then allowed to cool for 2 hours prior to use for the growth of synchronous cultures. An M2G starter broth culture was inoculated by carefully scooping two lines of bacteria from an inoculated plate with a sterile wooden pick and dipping the pick into 25 mL M2G media in an autoclaved 125 mL baffled flask. The flask was then lightly capped with aluminum foil and incubated at 30°C with continuous shaking at 210 rpm overnight.

The following day, 5 mL of the cells from the 25 mL M2G starter broth were diluted into 200 mL M2G media in a 1L autoclaved baffled flask. The flask was covered with aluminum foil and incubated at 30°C with continuous shaking at 210 rpm. The optical density at 600 nm ($OD_{600}$) was recorded every hour to measure the growth of the culture using an Ultraspec 10 spectrophotometer from Amersham Biosciences (Amersham, UK). To record measurements, the spectrophotometer was zeroed using a cuvette containing only M2G media. Then, a 500 µL aliquot of the diluted culture was placed into a disposable 1.5 mL polystyrene cuvette and the $OD_{600}$ measurement was recorded. The culture was incubated until the $OD_{600}$ was somewhere between 0.5 and 0.6, at which point 5 µL of the culture was pipetted onto a glass slide and visualized using phase microscopy to confirm the presence of both stalked and swarmer cells.

Next, the synchronization process was initiated by transferring 200 mL of the cell culture grown in the M2G media into autoclaved 25 mL ultracentrifuge tubes to constitute a total of 8 tubes. Cells were pelleted via centrifugation for 15 min at 7000 RCF at 4°C using a Fiberlite™ F20-12x50 LEX rotor and a Sorvall LYNX 4000 Superspeed Centrifuge. The supernatant was carefully discarded to remove predivisional cells. The cell pellet was resuspended in 5 mL cold M2G media using a serological pipet. A 2.5 mL aliquot of colloidal silica solution, which was twice filtered through a 0.22 µm nylon syringe filter and autoclaved, was added to each ultracentrifuge tube and homogenized by 15 sec of vigorous shaking. The silica-cell mixture was subsequently centrifuged for 35 min at 9700 RCF at 4°C. Following centrifugation, three distinct bands were observed, a bottom swarmer cell band, a middle predivisional cell band, and an upper stalked cell band. This separation is observed due to the differences in buoyancy of each cell type; stalked cells are much more buoyant than swarmer cells and thus rise to the top band when centrifuged with the colloidal silica solution. As a result, the various cell types were effectively

separated from one another. A Pasteur pipet was used to carefully remove the stalked and predivisional cell bands up to ~1 cm above the swarmer cell band. Each centrifuge tube was topped off with cold M2G and centrifuged for 10 min at 7650 RCF at 4°C. The supernatant was discarded, and the process was repeated two more times. Each cell pellet was resuspended in 20 mL cold M2G media in an autoclaved centrifuge tube. To visualize the success of the synchronization process, 5 µL of the resuspended cell pellet was visualized using phase microscopy to confirm the presence of only swarmer cells.

After the synchronization process was complete, the cells were centrifuged a final time for 10 min at 7650 RCF at 4°C and resuspended in an appropriate volume of 30°C M2G media so that the $OD_{600}$ was somewhere between 0.3 and 0.35. The resuspended cells were transferred to an autoclaved 125 mL baffled flask and incubated at 30°C with continuous shaking at 210 rpm until the desired $OD_{600}$ values for synchronous SM (0.4, 0.6, 0.8, and 1.0) were reached.

### 2.4: Isolation of *C. crescentus* spent media

Once the asynchronous or synchronous *C. crescentus* culture reached the desired $OD_{600}$ value, a 3-5 mL aliquot of the culture was removed, placed into an autoclaved ultracentrifuge tube, and centrifuged for 10 min at 7650 RCF at 4°C. The supernatant was poured into a sterile 0.2 µm vacuum filtration apparatus and filtered. The isolated SM was retrieved from the filtrate, aliquoted, and stored in autoclaved 500 µL Eppendorf tubes at -20°C.

### 2.5: Quantifying approximate protein concentrations in spent media

In order to quantify the approximate protein concentrations of each SM aliquot, a BCA assay was carried out. A commercial Pierce™ BCA Protein Assay Kit was obtained from ThermoFisher Scientific (Heysham, England). The kit contained reagent A (sodium carbonate,

sodium bicarbonate, sodium tartrate, and sodium hydroxide), reagent B (cuprous BCA complex), and several ampoules of 2 mg/mL BSA standards for external standard development.

First, reagents A and B were combined in 1:8 v/v ratio to produce the working reagent solution. Then, a set of standards was prepared using the provided BSA standard. The range that was used for this application was as follows: 0, 25, 125, 250, 500, 750, 1000, 1500, and 2000 µg/mL BSA. All standards were diluted using citrate buffer. In a 96 well microplate, 25 µL of each standard and SM aliquot was pipetted in triplicate followed by 300 µL of working reagent. The microplate was mixed thoroughly for 1 minute. The plate was then covered with aluminum foil and allowed to incubate for 1 hour at 37°C in an incubator with shaking turned off. Once incubation was complete, the plate was cooled to room temperature and analyzed with a plate reader at 562 nm. Each set of triplicate measurements of the standards were averaged and used to construct an external calibration curve ($R^2 > 0.999$) which was subsequently used to ascertain the approximate protein concentration in each SM sample.

**2.6: Nanoparticle and eco-corona characterization via dynamic light scattering (DLS)**

DLS measurements were collected using a Zetasizer Nano ZS from Malvern Panalytical (Malvern, PA). Prior to recording a measurement, the instrument was allowed to warm up for at least 30 minutes. Each sample was prepared in a disposable polystyrene cuvette which was rinsed three times with citrate buffer which had been filtered three times through a 0.2 µm nylon syringe filter. To measure the hydrodynamic diameter of a sample, a semi-micro cuvette with 1 cm pathlength was used. To measure the zeta potential of a sample, a macro cuvette with 1 cm pathlength was used and a Pd dip cell was inserted. The dip cell was thoroughly rinsed with Millipore water between each measurement. Each sample was prepared in triplicate directly in a cuvette by first diluting SM 1:1000 in citrate buffer and then adding an appropriate volume of

AgNPs to constitute a final volume of 1 mL with a concentration of 1 mg $L^{-1}$ for 10 nm AgNPs or 5 mg $L^{-1}$ for 40 nm AgNPs. The hydrodynamic diameter and zeta potential were recorded for each sample immediately after the addition of AgNPs and again after two hours of incubation at room temperature. Directly before recording a measurement, each sample was vortexed for 10 seconds and then inserted into the instrument. Each sample was analyzed at 25°C after 120 seconds of equilibration. The refractive index was set to 1.330 and an absorption at 633 nm was set to 0.010. Normal resolution processing mode was used to process all data. Zeta potentials were determined using the Smoluchowski equation.

### 2.7: Measuring AgNP dissolution kinetics via linear sweep stripping voltammetry (LSSV)

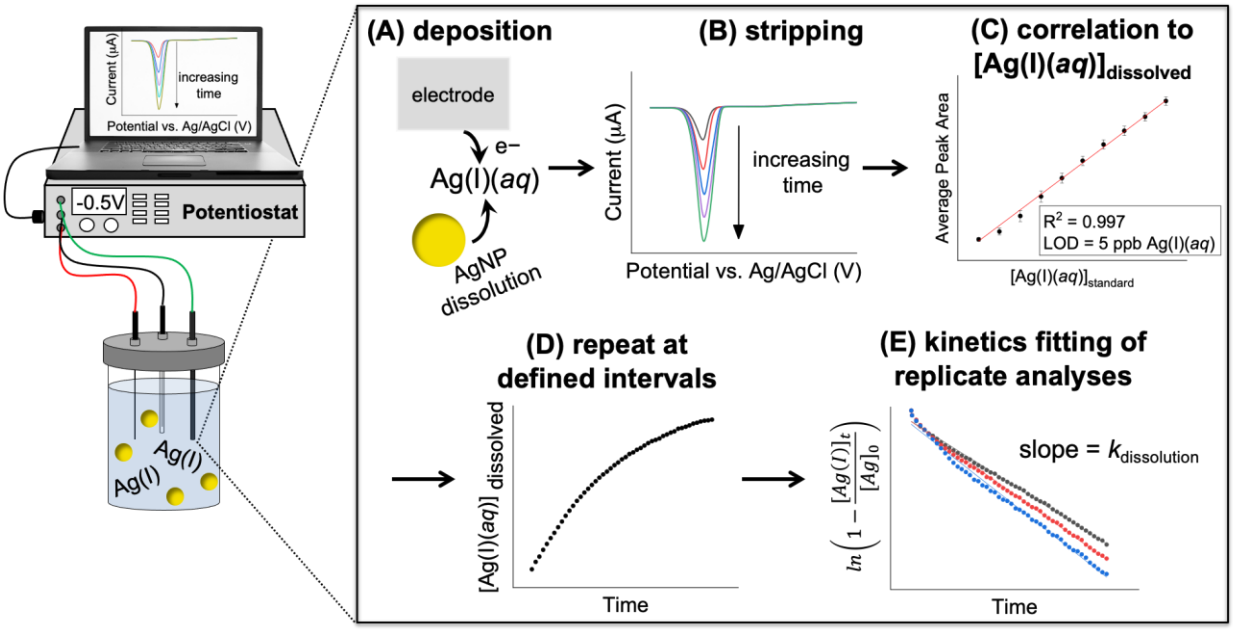


**Figure 3.** Linear sweep stripping voltammetry (LSSV) method which was employed to measure the dissolution kinetics of AgNPs in various solution conditions and determine the average first-order rate constant for a triplicate dissolution experiment.

The general workflow for a AgNP dissolution kinetics experiment by way of LSSV is shown in Figure 3. In general, Ag(I) dissolved from AgNPs is reduced at a glassy-carbon working electrode in a "deposition step" by holding the potential at -0.5 V vs. a Ag/AgCl

reference electrode (**Figure 3A**). Then, the potential is swept from -0.5 V to 0.35 V, oxidizing any deposited silver from the working electrode in a "stripping" step which generates an observable change in the current (**Figure 3B**). Measurements are repeated every 5 min for 2 hours. Dissolved Ag(I) concentrations are determined through correlation to a calibration curve (**Figure 3C**) and plotted with respect to time to obtain dissolution kinetic plots (**Figure 3D**). Kinetic plots can be fit to a first-order kinetic model to generate a rate constant, $k_{\text{dissolution}}$ (**Figure 3E**), according to:

$$\ln\left(1 - \frac{[Ag(I)]_t}{[AgNP]_i}\right) = -k_{dissolution} \quad (1)$$

where $[Ag(I)]_t$ represents the concentration of ionic silver at a specific time point while $[AgNP]_i$ represents the initial concentration of nanosilver.[64]

LSSV experiments were conducted with a BASi Epsilon EClipse potentiostat and a C-3 Cell Stand from Bioanalytical Systems, Inc. (West Lafayette, IN). A three-electrode system was used with a glassy-carbon macroelectrode (~3 mm) as the working electrode, a platinum wire as the counter electrode, and a Ag/AgCl electrode as the reference electrode. The working electrode was polished weekly with successive 15 µm, 3 µm, and 1 µm diamond polishes followed by a final 0.05 µm alumina polish. Additionally, the working electrode was polished daily with 0.05 µm alumina polish. Prior to insertion, the working electrode was bath-sonicated for 30 seconds in Millipore water to ensure any remaining alumina polish was removed. After polishing and cleaning, the electrodes were conditioned in the solution of interest by cycling from 0.35 V to -0.5 V at 0.3 V $s^{-1}$ for 200 cycles.

At the start of each working day, a 12-point matrix-matched calibration curve was generated. A working stock of 10 mg $L^{-1}$ silver standard solution was prepared in Millipore water

prior to the start of each calibration experiment. The calibration curve was generated by injecting consistent volumes of the silver standard working stock to vary the total $Ag(I)_{(aq)}$ concentration by 25 µg $L^{-1}$ from 0 µg $L^{-1}$ up to 500 µg $L^{-1}$. Upon each injection, five replicate LSSV measurements were recorded and averaged.

To conduct one run of a triplicate dissolution experiment, a solution of interest (citrate buffer or diluted SM) was first allowed to homogenize by rapid stirring and sparging with nitrogen for 10 minutes to achieve a final dissolved oxygen concentration of roughly 8.0 mg $L^{-1}$. The AgNP stock solution was bath-sonicated during these 10 minutes to ensure homogeneity. Then, an appropriate volume of AgNPs was added to the electrochemistry cell to constitute a final volume of 5 mL with a concentration of 1 mg $L^{-1}$ or 5 mg $L^{-1}$ for 10 nm and 40 nm AgNPs respectively. The solution was stirred for 30 seconds after the addition of AgNPs and then the first measurement was recorded. From thereon, a measurement was recorded every 5 minutes for 2 hours, totaling 24 individual measurements.

## Chapter 3: Qualitative evaluation of the *C. crescentus* eco-corona

To understand the formation of the *C. crescentus* eco-corona, it is first important to have a general idea of the biochemical makeup of the different SM aliquots. Since proteins are quite easy to detect even without a purification step and produced at higher concentrations with higher $OD_{600}$ values in the *C. crescentus* cell-cycle, we sought to measure the protein concentration in each SM aliquot. Additionally, the majority of research in the field of nanoparticle coronas focuses on protein coronas.[10,26,35,37,44] Thus, monitoring the relative concentrations of protein in SM aliquots is a good starting point for understanding the composition of *C. crescentus* eco-coronas.

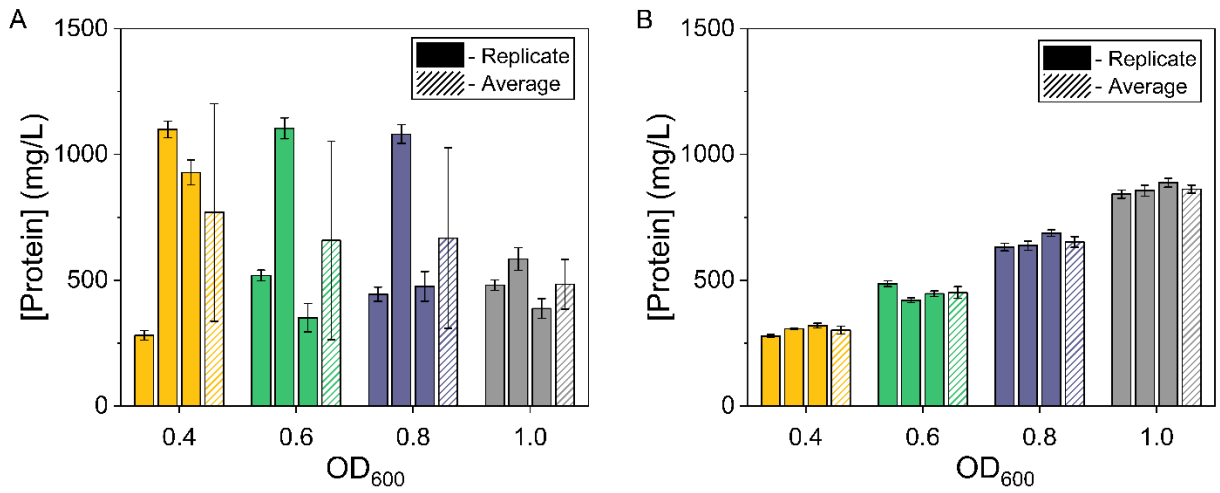


**Figure 4.** Protein concentrations in SM samples isolated at different $OD_{600}$ values from three replicate cultures of **(A)** asynchronous *C. crescentus* and **(B)** synchronous *C. crescentus*. Protein concentrations were determined via the BCA assay.

The two distinct cell types in the *C. crescentus* cell-cycle have distinct levels of protein output, so the protein concentration is expected to be correlated to the stage of cell development. That is, as a stalked and swarmer cell are produced via asymmetric division of a singular stalked cell, the amount of protein being produced in the bulk bacterial culture should increase as the $OD_{600}$ of the SM increases. However, in an asynchronous culture, where the bacteria are at

different cell cycle stages, no correlation between protein concentration and $OD_{600}$ is expected. Accordingly, using the BCA assay it was determined that asynchronous cultures of *C. crescentus* have wide variability of protein outputs when comparing across replicate cell cultures (**Figure 4A**, **Table A1**). There was no correlation between $OD_{600}$ and the protein concentration; at the smallest $OD_{600}$ the average protein concentration was 770 ± 430 mg/L while at the largest $OD_{600}$ the concentration was 480 ± 100 mg/L. Whether comparing the average protein concentrations across the various $OD_{600}$ samples (dashed bars, **Figure 4A**) or trends within each replicate of the asynchronous cell culture (solid bars, **Figure 4A**), there is no clear correlation between the stage of cell growth and the protein concentration.

The same assay was repeated with the synchronous *C. crescentus* cultures to determine whether the protein concentrations were correlated with the stage of cell development and the transition between the two cell morphotypes. As expected, there is a strong positive linear relationship between the amount of protein produced and the $OD_{600}$ value, or the point in the *C. crescentus* cell-cycle at which time the SM aliquot was obtained. At $OD_{600}$ 0.4 the average protein concentration was 300 ± 20 mg $L^{-1}$, while at the highest $OD_{600}$ the average protein concentration was 860 ± 20 mg $L^{-1}$ (**Figure 4B**, **Table A2**). In addition to the linear relationship, the protein concentrations were highly reproducible across replicate cultures with a consistent standard deviation of 20 mg $L^{-1}$ protein. This suggests that although a complex mixture of biomolecules is excreted by the *C. crescentus*, the total concentration of protein is highly reproducible at the various timepoints in the cell cycle. This is also confirmed by visualizing the uniformity among each individual replicate collected at a specific $OD_{600}$. Unlike the asynchronous cultures where there were extremely high levels of variance between each of the

replicates, the synchronous cultures present concentrations that are all within the standard error of one another.

This data suggests that the general concentration of protein excreted by *C. crescentus* increases with cell growth. Although only protein concentrations can be determined with the BCA assay, published metabolomics data shows significant correlation between protein concentrations and the concentrations of other biomolecules, like metabolites.[53] This means that there may be broader implications related to how the composition and concentration of metabolites excreted by *C. crescentus* correlates with cell cycle in our model.

With a general understanding of the degree of biomolecular complexity in each SM aliquot, the formation of *C. crescentus* eco-coronas on AgNPs was examined using DLS. To do so, both the hydrodynamic diameter ($d_H$) and polydispersity index (PDI) of AgNPs in the presence of SM and diluted in citrate buffer were measured (**Table A3-A4**). By leveraging the inverse relationship between Brownian motion and particle size, DLS is able to determine the average particle size in a sample. In DLS, Brownian motion is tracked by monitoring changes in the scattering pattern and intensity of a laser directed onto the sample as a function of time. For smaller particles, the scattering pattern and intensity will become quickly decorrelated as the particles move due to Brownian motion. A correlation function is used to measure the rate at which the scattering becomes decorrelated to determine the size of the particle. The overall surface charge of AgNPs can also be determined using zeta potential measurements, which correlate the scattering intensity with time as the particles migrate under an applied electric field.[65]

Upon formation of an eco-corona several changes are expected relative to the SM itself, including a slight increase in the size (consistent with the addition of an adsorbed biomolecule

layer), a decrease in the PDI (due to steric stabilization of the colloidal suspension by the biomolecules), or a decrease in the zeta potential (due to charge screening or displacement of the AgNP stabilizing ligands by the biomolecules).

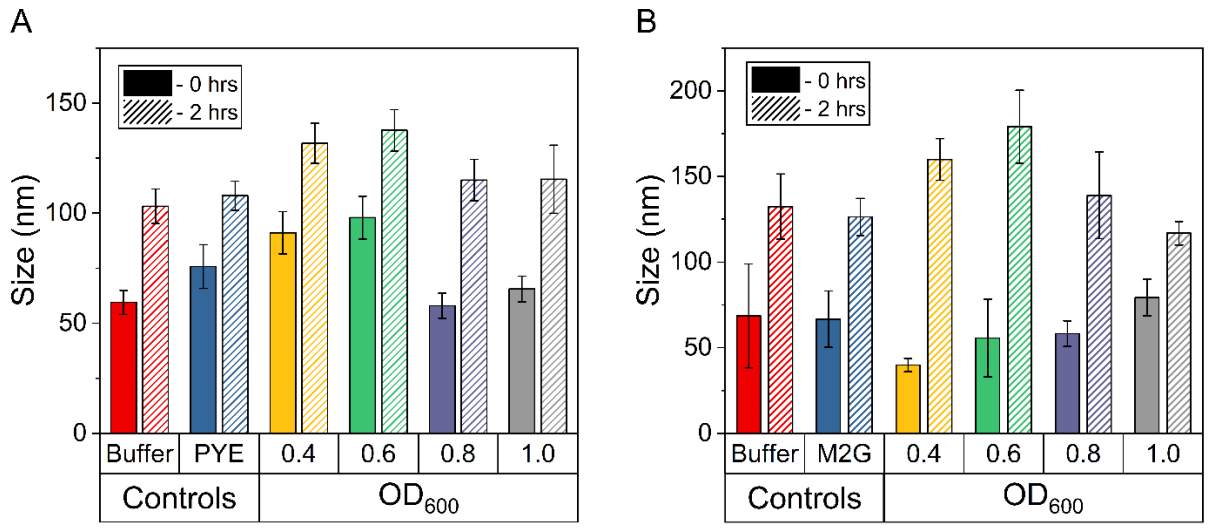


**Figure 5.** Hydrodynamic diameter of 10 nm AgNPs before and after 2 hr incubations with **(A)** asynchronous *C. crescentus* SM and **(B)** synchronous *C. crescentus* SM.

First, the $d_H$ of the 10 nm AgNPs was measured in two control solutions, the citrate buffer and the M2G media. Both controls have a higher $d_H$ than expected, thus suggesting some aggregation of the AgNPs in these solution conditions. In both cases, the size of the particles increases over time, suggesting even further aggregation over the 2h incubation period (which was chosen to mimic the time scale of later dissolution studies). The citrate buffer which was used for all of the DLS experiments conducted includes 15 mM NaCl which has been shown to induce aggregation of AgNPs.[8] Additionally, in the samples incubated with media, there are many different ionic species present which are required for bacterial growth. These species are likely inducing aggregation in a similar way to the NaCl in the citrate buffer. In particular, the divalent cations $Ca^{2+}$ and $Mg^{2+}$ in the M2G media can induce significant aggregation.[8] These changes in size were immediately attributed to aggregation due to the broadening of the LSPR

band visible in UV-Vis (**Figure A4**). Taken together, it is clear that significant aggregation is occurring upon incubation of AgNPs with *C. crescentus* SM as well as due to the buffer conditions.

Next, 10 nm AgNPs were combined with SM isolated at different $OD_{600}$. In all cases, the size of the AgNPs increased considerably over the 2 hr incubation period. For instance, the AgNPs mixed with SM isolated at $OD_{600}$ 0.6 had an initial $d_H$ of 100 ± 10 nm and after 2 hrs the $d_H$ had increased to 140 ± 10 nm (**Figure 5A**, **Table A5**). This is a large increase of approximately 40 nm which is attributed to aggregation of the particles. However, since the initial $d_H$ was larger than the expected $d_H$ it is possible that there were already aggregates present which were subsequently coated with the *C. crescentus* eco-corona, or that the *C. crescentus* eco-corona formed almost instantaneously and induced AgNP aggregation. Compared to the controls, the SM samples isolated at $OD_{600}$ 0.4 and 0.6 had larger initial $d_H$ values which suggests the addition of the SM induced additional aggregation, which ultimately led to larger aggregates after 2h. In contrast, the SM samples isolated at $OD_{600}$ 0.8 and 1.0 had smaller initial $d_H$ values than the controls which suggests the addition of the SM initially stabilized the AgNPs, although after 2h the AgNPs still formed rather large aggregates.

Likewise, incubation of 10 nm AgNPs with synchronous SM mixtures led to similar AgNP aggregation, with some differences. First, compared to the controls, the initial $d_H$ of the AgNPs was generally smaller, suggesting that the biomolecules in the SM imparted some initial colloidal stability (**Figure 5B**, **Table A7**). Interestingly, the $d_H$ of the AgNPs appears to increase with increasing $OD_{600}$. Since the protein concentration in the MS isolate also increases with $OD_{600}$, this result suggests that perhaps more protein adsorbed to the AgNPs when higher concentrations of protein were in the SM sample. However, after 2 hours, all SM samples were

significantly aggregated; although, OD 0.8 and 1.0 samples have smaller aggregate sizes which might suggest that the higher protein concentrations in these samples led to more uniform size distributions of the aggregates. Regardless of these intricacies, the size of all AgNP-SM mixtures increased suggesting AgNP aggregation and a strong interaction between the *C. crescentus* biomolecules and the AgNPs which become even clearer upon looking at the raw size distributions themselves (**Figure A5**-**A8**).

Unfortunately, DLS has a limit of detection of around 10 nm, which is the precise size of AgNPs used throughout the majority of this work.[66] Thus, the $d_H$ data is not entirely representative of the actual sizes of the AgNPs reported by the manufacturer and obtained via transmission electron microscopy (10 ± 2 nm). This issue is exacerbated by the buffer conditions—it is widely accepted that high salt conditions can induce aggregation, thus effectively increasing the apparent size of the AgNPs. This aggregation is visible in both asynchronous and synchronous cultures evidenced by the increase in size for both control measurements. Although not conclusive, the trends associated with the size data can shed light on the formation of *C. crescentus* eco-coronas when combined with observations of PDI and zeta potential measurements.

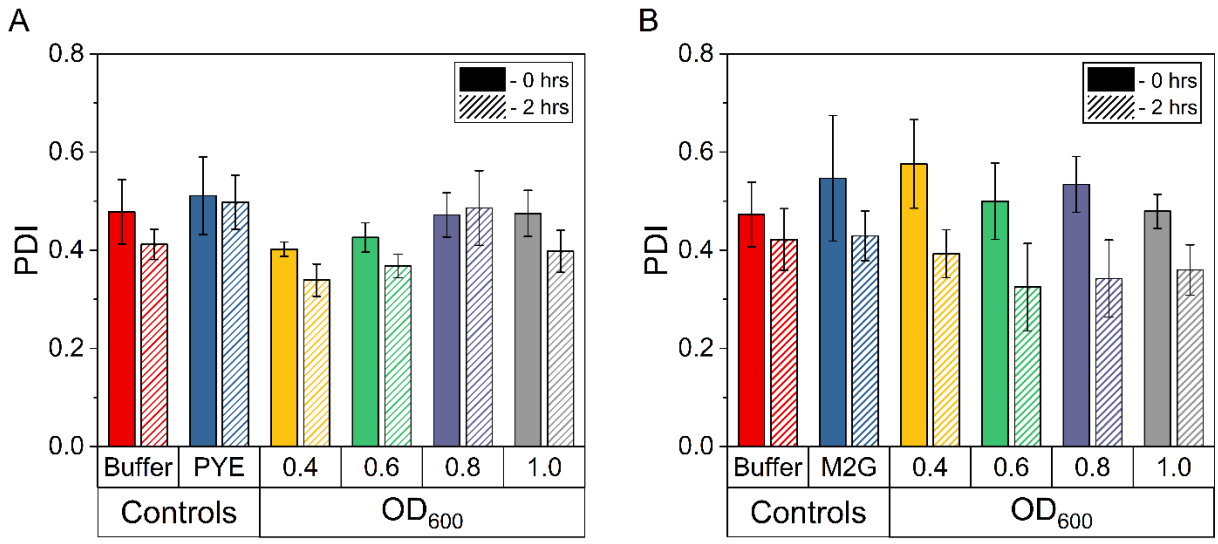


**Figure 6.** PDI of 10 nm AgNPs before and after 2 hr incubations with **(A)** asynchronous *C. crescentus* SM and **(B)** synchronous *C. crescentus* SM.

In both the asynchronous and synchronous case, the PDI of the 10 nm AgNPs slightly decreased over time in the control solutions (buffer and media). In the presence of SM isolated from the asynchronous cultures, the PDI of the AgNPs also generally decreased over the 2h incubation period (**Figure 6A**). A decrease in the PDI of the AgNPs suggest formation of a more homogeneous mixture and a decrease in the size distribution of the AgNP aggregates. In the presence of SM isolates from the synchronous cultures, the PDI of the AgNPs decreased much more considerably over the 2h incubation period (**Figure 6B**). Although in both cases the SM plays a generally stabilizing effect, it is much more prevalent in the synchronous SM samples. This is consistent with our observations from the $d_H$ measurements which show that a more uniform size distribution of aggregates is formed in the presence of the synchronous SM isolates. These results suggest that the unique mixtures of biomolecules in the synchronous and asynchronous *C. crescentus* SM has a unique influence on AgNP colloidal stability that may be related, at least in part, to the concentrations of specific biomolecules in each mixture. Overall, measurements of the $d_H$ and PDI suggest an interaction between the SM biomolecules and the

AgNPs, however, due to the fact that there are varying levels of aggregation present, these measurements alone are not decisive enough to confirm the formation of the eco-corona. Thus, zeta potential measurements were performed as an additional tool to evaluate whether the *C. crescentus* eco-coronas formed.

As previously mentioned, due to the buffer conditions which inherently biased aggregation of the particles, zeta potential was analyzed in hopes of confirming the formation of both the asynchronous and synchronous *C. crescentus* eco-corona (**Figure 7**). Generally, the formation of an eco-corona results in a decrease in the magnitude of the measured zeta potential either due to charge screening or by the replacement of capping agents (citrate in the case of AgNPs) with biomolecules. If the latter occurs, the measured zeta potential is expected to be similar to the measured zeta potential for the SM itself.

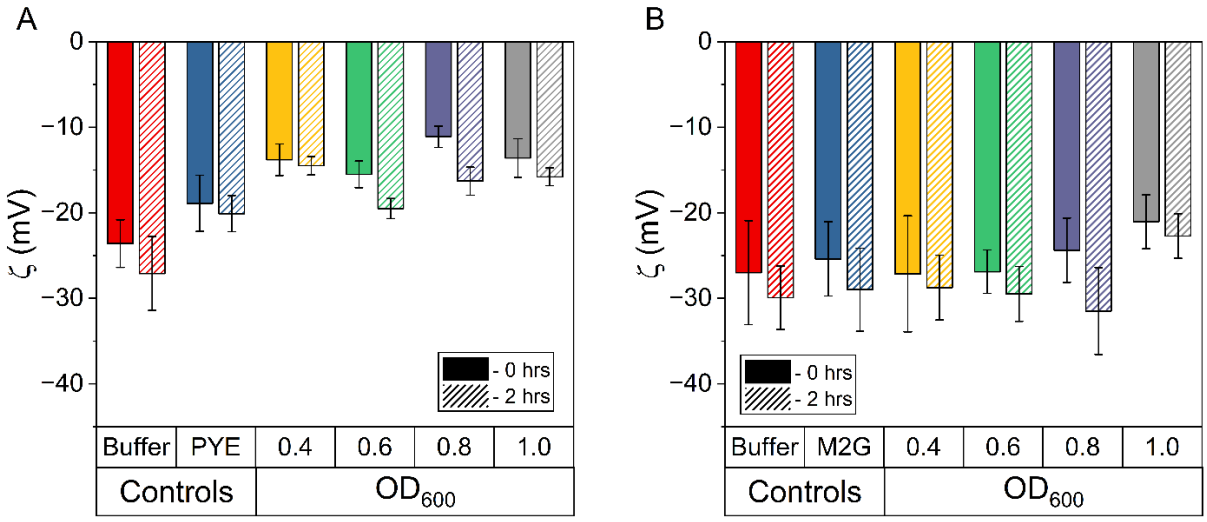


**Figure 7.** Zeta potential of 10 nm AgNPs before and after 2 hr incubations with **(A)** asynchronous *C. crescentus* SM and **(B)** synchronous *C. crescentus* SM.

Compared to the controls, the AgNPs incubated with the asynchronous SM had a smaller zeta potential, indicative of charge screening by the biomolecules (**Figure 7A**). In this

phenomenon, charged particles (or biomolecules in this case) can surround a colloid (AgNP) thus resulting in an effective "shielding" of the AgNP surface and a decrease in zeta potential. All asynchronous SM samples show this characteristic decrease in zeta potential after incubation with SM, thus suggesting the formation of these asynchronous eco-coronas. For the synchronous *C. crescentus* SM, the zeta potential decreases most significantly for the $OD_{600}$ 1.0 sample, suggesting perhaps greater adsorption of biomolecules to the AgNP surface due to the higher protein concentration at that $OD_{600}$ (**Figure 7B**). At first glance, the zeta potential measurements seem to suggest that the asynchronous SM may adsorb more strongly to AgNPs than the synchronous SM. However, zeta potential measurements are also affected by aggregation and zeta potential values with magnitudes ≤ 20 mV are indicative of aggregation. Thus, the zeta potential measurements are consistent with the $d_H$ and PDI measurements which suggest more significant aggregation in the presence of asynchronous SM than in the presence of asynchronous SM. Although the data for the 10 nm AgNPs was the primary data presented here, the same process was conducted for the 40 nm AgNPs with extremely similar results. A full set of triplicate DLS measurements for 40 nm AgNP incubations with both asynchronous and synchronous SM has not yet been collected, however, one set of replicates for both was completed (**Figures A1-A3**, **Tables A6 and A8**). Based on this data, the same trends stand true for both the asynchronous and synchronous and thus we posit that both the asynchronous and synchronous *C. crescentus* eco-coronas formed for the 40 nm particles as well.

When the size, PDI, and zeta potential data are all taken together, it becomes clear that biomolecules from both the asynchronous and synchronous *C. crescentus* cultures strongly interacted with the AgNPs, inducing aggregation and likely forming an eco-corona. Both controls also show AgNP aggregation, however, it is important to understand that AgNPs readily

aggregate in most aqueous solutions, especially those that contain large amounts of ionic substitutents.[27] This is well understood and is likely what is occurring in both controls. Even still, the aggregation induced by the SM isolates is unique from the controls and shows different patterns with SM $OD_{600}$ for synchronous compared to asynchronous cell cultures.

## Chapter 4: Impact of the *C. crescentus* eco-corona on AgNP dissolution

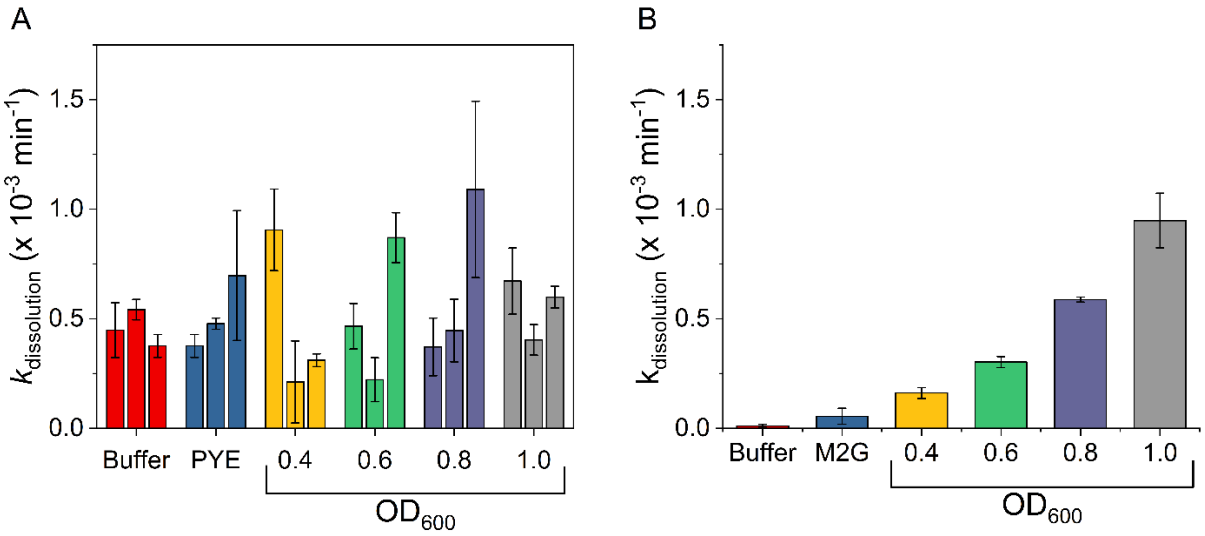


**Figure 8.** Dissolution rate constants of 40 nm AgNPs in the presence of **(A)** asynchronous SM or **(B)** synchronous SM determined by LSSV. The initial concentration of AgNPs was 5 mg $L^{-1}$ and each sample was prepared by diluting SM 1:1000 in citrate buffer of pH 5.3.

After characterizing the asynchronous and synchronous *C. crescentus* eco-coronas and their interaction with AgNPs, the impact of these eco-coronas on the dissolution behavior of AgNPs was investigated. Although the identities of the components of the various SM mixtures are unknown, combining published metabolomics data with the results from the BCA assay described in Chapter 3 provides some understanding of the biomolecular diversity of the SM. Metabolomics data suggests that there is a link between the level of excreted protein and the other metabolites in a SM sample; that is, the more uniform the amount of protein that has been excreted from replicate to replicate, the more likely that the other excreted biomolecules in these replicates are uniform in composition and concentration.[52,60] Since the composition of the SM mixtures are what dictates the composition of the eco-corona, and the composition of the eco-corona is what dictates the AgNP dissolution behavior, we would expect to see a link between the degree of uniformity in excreted protein concentrations and overall dissolution behavior.

Using the highly variable and non-reproducible asynchronous SM mixtures expectedly led to inconsistent and fluctuating dissolution rate constants for the 40 nm AgNPs (**Figure 8A**). For instance, within the 0.8 $OD_{600}$ SM sample isolated from asynchronous cultures, two of the trials have similar dissolution rate constants, $0.4 \pm 0.1 \times 10^{-3}$ $min^{-1}$ and $0.4 \pm 0.1 \times 10^{-3}$ $min^{-1}$, while the third is much larger than the other two with a value of $1.1 \pm 0.4 \times 10^{-3}$ $min^{-1}$ (**Table A9**). The same pattern holds true for each of the asynchronous SM samples, thus making a trend nearly impossible to draw. This aligns with the variation in protein concentrations in the SM and in the heterogeneous interactions of SM biomolecules with the AgNPs discussed in Chapter 3.

It is for this reason that the synchronization process was of utmost importance for gathering meaningful information about the correlation (if any) between eco-corona composition and AgNP dissolution. Approximately 15% of the *C. crescentus* metabolome varies with cell-cycle and the $OD_{600}$ is a strong measure of cell-cycle stage once a culture is synchronized.[53] This allows SM mixtures isolated at specific $OD_{600}$ to be correlated to particular points in the cell-cycle and to specific biomolecules excreted at that stage of the cell-cycle, which can be determined using 'omics'-based techniques (i.e., proteomics, metabolomics, or lipidomics). If SM isolated at a specific $OD_{600}$ elicits a unique change in AgNP dissolution properties, specific biomolecules may play a significant role in modulating AgNP redox chemistry, which has important implications for understanding the environmental fate and reactivity of AgNPs.

Synchronous cultures of *C. crescentus* produced more reproducible protein concentration leading to the formation of more uniform eco-coronas with AgNPs (Chapter 3). For this reason, a direct trend between the stage of *C. crescentus* cell growth and AgNP dissolution rate was expected. Preliminary data for the dissolution rates of 40 nm AgNPs incubated with synchronous *C. crescentus* SM shows a strong relationship between $OD_{600}$ and AgNP dissolution

(**Figure 8B**). Although only one cell culture replicate of this dissolution experiment has been completed, there is a clear trend that matches what is expected for this system. Specifically, as the cell-cycle stage ($OD_{600}$) progresses, there are unique eco-coronas that form leading to unique dissolution behavior at each level of cell growth. In particular, we see that the highest measure of cell growth ($OD_{600}$ 1.0 OD) has the largest rate of AgNP dissolution with an average of $24 \pm 3 \times 10^{-3}$ $min^{-1}$ (**Table A10**).

This aligns with literature data which inform that at these later stages in the cell-cycle there is a phenomenon known as the "swarmer storm". In this phase, the bacterial population begins to asymmetrically divide producing a vastly larger proportion of swarmer cells than at any other point in the cell-cycle.[51,52] As a result of this unique moment of cell growth, there are many different biomolecules excreted, including not just proteins, but also metabolites, lipids, carbohydrates, signaling molecules, etc. This is the reason that we see such an increase in the dissolution at this later cell-cycle stage as opposed to earlier cell growth. There is one predominant hypothesis as to why this sort of trend would arise—the formation of an eco-corona is not always entirely uniform around an entire AgNP, thus leaving certain points on the AgNP surface vulnerable to oxidative dissolution. This is especially pertinent due to the role that Ag(I) diffusion plays in this process. One can imagine something like a protein completely coating the AgNP surface, which would decrease $O_2$ diffusion to the surface and Ag(I) diffusion from the surface and slow further dissolution. On the other hand, smaller biomolecules like nucleic acids or carbohydrates may leave some of the AgNP surface exposed allowing for rapid $O_2$ diffusion to the surface and Ag(I) diffusion from the surface, and enhance dissolution. Based on the trends in the 40 nm AgNP synchronous dissolution compared to the absence of a trend in the 40 nm AgNP asynchronous dissolution, a link between cell growth, biomolecule concentration, and

dissolution behavior begins to be revealed. However, the aforementioned hypothesis that suggests AgNP dissolution is most strongly dictated by Ag(I) diffusion remains to be evaluated. This hypothesis also aligns well with the widely understood first-order kinetic model of AgNP dissolution. To validate this assumption, both first and second order kinetic curves were plotted (**Figure A9-A12**).

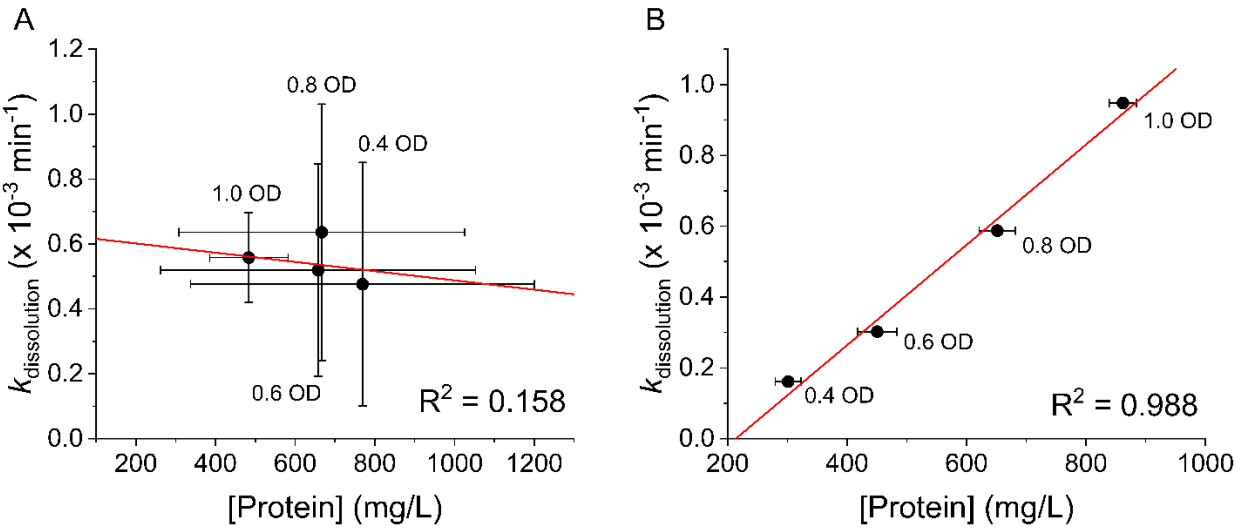


**Figure 9.** Correlation between dissolution rate constant for 40 nm AgNPs and **(A)** asynchronous SM protein concentrations ($R^2$ = 0.158) or **(B)** synchronous SM protein concentrations ($R^2$ = 0.988). The initial concentration of AgNPs was 5 mg $L^{-1}$ and each sample was prepared by diluting SM 1:1000 in citrate buffer of pH 5.3.

Correlation plots were created to begin to look at the relationship between protein concentrations in each SM mixture and the average dissolution rate of AgNPs. As expected, there is no correlation between protein concentration and AgNP dissolution rate for the asynchronous cell culture. Instead, there is an extremely weak negative linear relationship between protein concentration and dissolution rate (**Figure 9A**). When this same plot is constructed with the synchronous SM, a strong positive linear relationship between the two variables is revealed (**Figure 9B**), and suggests that the protein concentration strongly modulates the dissolution of 40 nm AgNPs. Importantly, this relationship remains true for all points in the

cell-cycle. This does not entirely align with the described diffusion hypothesis. However, due to the lack of currently understood mechanistic models for biomolecule-mediated AgNP dissolution and the fact that only one replicate for this system was completed, we cannot completely reject this hypothesis.

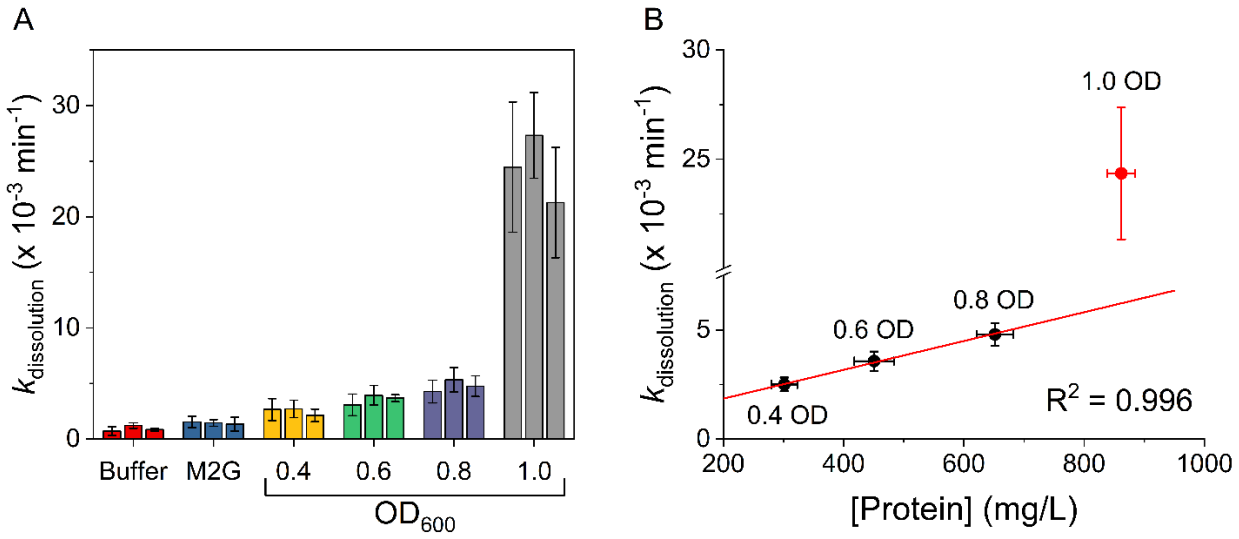


**Figure 10. (A)** Dissolution rate constants of 10 nm AgNPs with synchronous SM determined by LSSV. **(B)** Correlation between dissolution rate constant for 10 nm AgNPs and synchronous SM protein concentrations. The correlation for OD 0.4 – 0.8 is 0.996. The initial concentration of AgNPs was 1 mg $L^{-1}$ and each sample was prepared by diluting SM 1:1000 in citrate buffer of pH 5.3.

In order to understand the role that the size of the particle plays in this complex process, this same process was carried out with 10 nm AgNPs and synchronous SM due to the absence of any clear trends with the asynchronous SM data (**Figure 10**). Due to the fact that this process was completed in triplicate with the smaller particle size, there is a much more pronounced trend. The first main point of interest is the reproducibility among each unique treatment group. For instance, the AgNP dissolution rate constants determined in the presence of a respective 0.4 OD SM sample are all within one standard deviation (**Figure 10A**). These values are $2.7 \pm 0.9 \times 10^{-3}$ $min^{-1}$, $2.7 \pm 0.8 \times 10^{-3}$ $min^{-1}$, and $2.1 \pm 0.6 \times 10^{-3}$ $min^{-1}$ respectively (**Table A11**). As expected, the reproducibility in this data matches the reproducibility in synchronous *C.*

*crescentus* excreted matter. Even further there is a strong linear relationship between 10 nm AgNP dissolution rates and the protein concentration from SM isolated at $OD_{600}$ 0.4 through 0.8 (**Figure 10B**). At $OD_{600}$ 1.0, the AgNP dissolution rate constant increases significantly and is no longer correlated to the protein concentration. This trend suggests that unlike the dissolution of 40 nm AgNPs which were only linked to the protein concentration of the synchronous SM, the smaller 10 nm AgNPs may be influenced by other biomolecules present at high concentration in the $OD_{600}$ 1.0 SM.

This idea fits in quite well with the diffusion hypothesis that was put forth earlier; proteins are quite dynamic and undergo many conformational changes which would, when part of an eco-corona, likely decrease the bare AgNP surface through these conformational changes. As a result, there is a much lower chance of oxidative dissolution at this exposed surface due to decreased chance of diffusion. This would result in lower dissolution rates in timeframes where there is predominantly protein adsorbed on the AgNP surface.

Instead, there are more than 400 metabolites that exhibit concentration changes as a function of cell-cycle stage.[53] Three of these compounds that would not be detected via BCA assay but are most certainly playing a large role in constructing the *C. crescentus* eco-corona at later OD values are c-di-GMP, adenosine monophosphate (AMP), and GDP-L-fucose.[67] These three compounds were selected from a larger *C. crescentus* metabolomics database due to their concentrations being initially low and rapidly increasing at the G2 → G1 cell-cycle transformation. The aforementioned "swarmer storm" at OD 0.85-0.90 is the point in the cell-cycle where we see the linear relationship between dissolution rate constant and OD disappear.

This too makes sense considering these three aforementioned metabolites as they are one of two things—signaling molecules which dictate the asymmetric division process or critical

nucleotides for swarmer cell growth.[60,68] Therefore, they would not be produced by the bacteria until directly before the point that they are needed, at which time they are produced in high concentrations. Thus, we propose that the eco-corona formed from SM isolated at earlier stages of cell growth ($OD_{600}$ 0.4 through 0.8) is predominantly composed of proteins, whereas at later stages it is also composed of these signaling molecules and nucleotides. This hypothesis aligns with the specific trends observed in all of the data presented for the synchronous eco-coronas; there appears to be two distinct trends—one for the bacterial populations of stalked cells containing mostly proteins ($OD_{600}$ 0.4 through 0.8) and one for the populations of majority swarmer cells containing mostly metabolites, nucleotides, and signaling molecules ($OD_{600}$ 1.0). Even further, this would explain the linear relationship between dissolution rate constant and OD until the point at which these three compounds begin to be produced at high concentrations.

## Chapter 5: Conclusions and Future Directions

The goal of this work was to explore the formation of complex eco-coronas using *C. crescentus* as a means by which to obtain eco-coronas. Rather than looking at the extremes of simplified eco-coronas or *in vivo* coronas, this study seeks to fill in the absence of information regarding complex eco-coronas. The work first employed a method for synchronization and subsequent isolation of *C. crescentus* SM. The protein concentrations of these SM mixtures were analyzed using a BCA assay; this revealed that synchronous SM mixtures had highly reproducible protein yields which increased in concentration linearly with cell growth. This suggests that synchronization is an effective means by which to isolate useful SM mixtures unlike the traditional asynchronous culturing processes.

Building upon previous work in the Riley Lab which used asynchronous *C. crescentus* SM mixtures to derive eco-coronas to evaluate the reactivity of 40 nm AgNPs, this work aimed to expand our knowledge of how AgNP size alters interactions with *C. crescentus* eco-coronas. First, characterization of the eco-coronas themselves was conducted using DLS. Using three different factors—namely size, PDI, and zeta potential—the formation of the *C. crescentus* eco-corona on both 10 and 40 nm AgNPs was confirmed. Due to the buffer conditions that were necessary for the electrochemistry conducted in this project, there was clear evidence of large-scale aggregation which made characterization of the eco-coronas themselves difficult.

Then, AgNP dissolution behaviors were analyzed as a function of cell growth via LSSV. This analysis revealed that there were two distinct trends based on the size of the particles used. For larger particles (40 nm), the dissolution behavior of the particles followed the trend in SM protein concentration very strongly. Whereas for smaller particles (10 nm), the dissolution behavior deviated from a strict dependence on SM protein concentration at later stages of cell

growth. These results suggest that particle size is a much more important factor in this field of study than previously anticipated. In general, this work expanded the understanding of how the composition of the eco-corona affects AgNP dissolution not only in a cell-cycle dependent manner

Although this work successfully posits evidence of eco-corona modified AgNP dissolution, it does not have grounds for confirming the mechanism of this modification. One reason for this is the lack of characterization that has been done on the *C. crescentus* SM itself. Moving forward with this project, it is of utmost importance to perform metabolomics on the SM mixtures. Although Swarthmore does not have access to much of the instrumentation nor methodology required for this sort of an analysis, finding an external institution that could assist with this would be instrumental in moving this project along from this point. Using high resolution liquid chromatography-mass spectrometry (LC-MS), an effective separation and identification of the components of *C. crescentus* SM can be completed. With better understanding of the identities of these compounds and their respective concentration in each SM mixture, we can begin to concretely understand the behaviors that we are observing.

To this same point, the characterization of the eco-corona conducted in this work is unfortunately not as robust as other studies conducted with simpler protein coronas. There are several reasons for this mainly related to the citrate buffer utilized in all of the DLS studies containing large amounts of ions which are required for the electrochemical experiments carried out. The development of other characterization techniques would provide an opportunity to study this system in parallel with the electrochemical experiments. However, these techniques like LC-MS and capillary electrophoresis (CE) do not have well-defined methods for the analysis that we are conducting. For this reason, it is likely that the ionic strength of the buffer must be reduced

for the DLS experiments in order to more confidently confirm the formation of *C. crescentus* eco-coronas.

Beyond studying dissolution behavior, which is just one of the important transformations that AgNPs undergo in the environment, this research can be applied to a much more specific understanding of eco-corona modified bacterial toxicity. Although many believe that AgNPs are antibacterial due to the dissolution of nanosilver into ionic silver, there is also research suggesting that this mechanism actually comes from the attachment of an AgNP to a bacterial cell wall. Therefore, another potential area of study that could be further explored (and currently is in the Riley Lab) is the toxicity of AgNPs to *C. crescentus*. This is especially pertinent given the enhanced dissolution shown in this work; if the dissolution is where this toxicity originates, there is a clear environmental concern.

Finally, AgNPs are just one example of the much broader ENM classification. There are numerous other systems that could be studied from this same lens to expand not only our understanding of the alteration of AgNP behavior, but also other ENM types. For instance, the model system and experimental workflow developed here could be applied to AgNPs with varying shape or surface coating or to other ENM compositions. AgNPs are not the only noble metal nanoparticle with antibacterial properties; in fact, gold nanoparticles (AuNPs) are also commonly used for their antibacterial properties. For this reason, it would be very beneficial to expand our knowledge to other types of noble metals ENMs.

## Acknowledgments

I would first like to thank my wonderful advisor, Dr. Kathryn Riley. You were the first professor I ever had the privilege of taking a course with at Swarthmore. As someone who had no intention in studying chemistry, the passion that you held for teaching the subject pushed me to find a love in this field! You have done more for me than I think you understand—from giving life advice to encouraging me when experiments did not go as planned, I do not think that I would be the person that I am today without you. There is no way to thank you enough for what you have done for me. I cannot wait to put forward what you have taught me as I go down the road of becoming a professor.

Next, I would like to thank all of the members of the Riley Lab. Casey Jordan—thank you for helping me with all things Origin and for keeping me sane while we both applied for PhD programs this past fall; Michael Caprise—you are such a joy to be around and I appreciated having another "senior citizen" alongside me in this last stretch; Mary Garcia-Barrios—from being my physical chemistry lab partner to now, it has been an absolute joy getting to know you! I cannot wait to see the amazing pedagogical work that you do; Moji Oludare—you are such a fun friend to have and I know you are going to do great things with this project; Iris Barone—I appreciate the kind energy that you bring into any space that you enter and cannot wait to see where you end up; Ritika Rajamani—I loved having someone to talk all things K-Pop with, I know that you will succeed no matter what path you decide to go down!

Every member of the Swarthmore Chemistry and Biochemistry department has been instrumental in my success, however, I would like to acknowledge a few that have been especially important. I am thankful to the members of my committee, Drs. Remi Beaulac and Sara Sohail, for their kind and encouraging words throughout the course of this thesis. I would

like to thank Drs. Kathleen Howard and Liliya Yatsunyk for always taking the time to meet with me whenever I needed assistance on anything chemistry (coursework, PhD applications, funding, etc); you have both been pivotal aspects of my time at Swarthmore. Finally, I would like to thank Dr. Maria Gallagher, Kelly Ambruso, and Lori Sonntag for their advice in applying to PhD programs and their general kindness throughout my time in their lab sections as their TAs.

I would also like to thank each member of The Wifedom—Sara Yun, Johanna Lee, Sophie Engels, and Linnea Holy—for their excellent company and for letting me ramble on about my project! You are all such lovely people, and I am so lucky to have each of you in my life. I would like to thank José Eduardo Valdivia Heredia, Lucia Navarro, Giselle Vigil, and Carlee Márquez for keeping me sane throughout my time at Swarthmore; I know you will all do amazing things for fellow FLI students in the future. Additionally, I would like to thank Taylor Morales, Jada Ruiz, Kira Esguerra, and Harmony Sweetgrass Sigler for all of their help getting to this point. You have all been invaluable resources when I felt lacking, and for that I cannot thank you each enough. I would also like to thank Kaitlyn Tran for her continuous support during my late nights in the lab and throughout my last two years at Swarthmore.

Finally, I would like to thank my mother and father for their constant support in this endeavor. It has not been easy being so far from them, but getting the opportunity to talk to them on FaceTime each and every day has been something I do not take for granted. Being the first person in my family to graduate from any institution at all is an immense privilege and I am so lucky to be able to put forward all that they have taught me.

To anyone that was not explicitly mentioned, you are valued, and I couldn't have done this without you! I love and appreciate each and every person that I had the chance to know during my time at Swarthmore. Thank you all from the bottom of my heart!

# Appendix

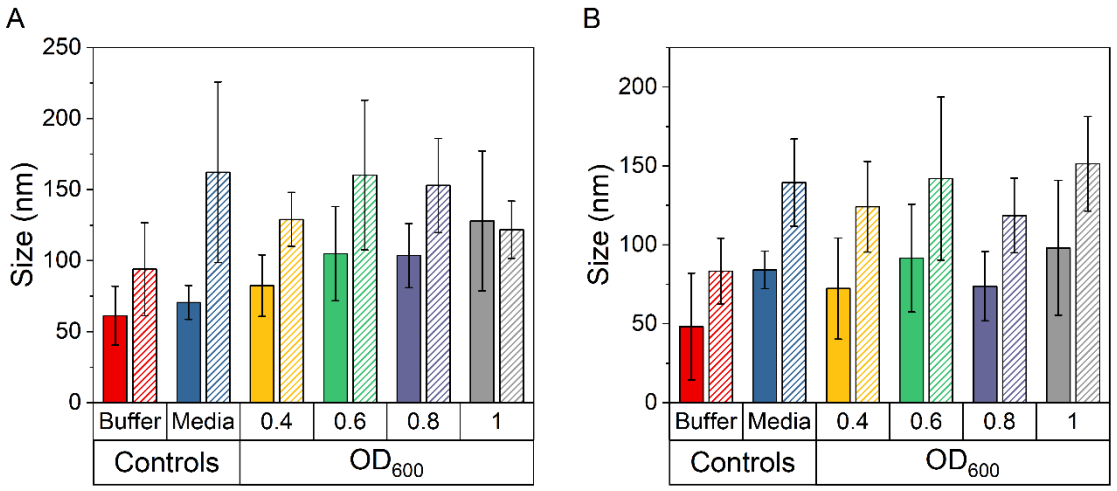


**Figure A1.** Hydrodynamic diameter of 40 nm AgNPs before and after 2 hr incubations with **(A)** asynchronous *C. crescentus* SM and **(B)** synchronous *C. crescentus* SM**.**

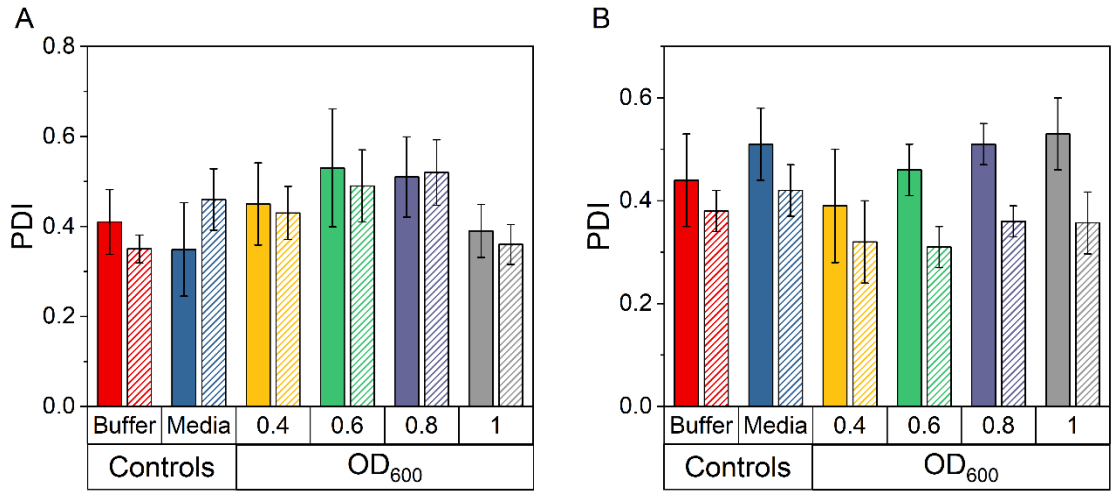


**Figure A2.** PDI of 40 nm AgNPs before and after 2 hr incubations with **(A)** asynchronous *C. crescentus* SM and **(B)** synchronous *C. crescentus* SM**.**

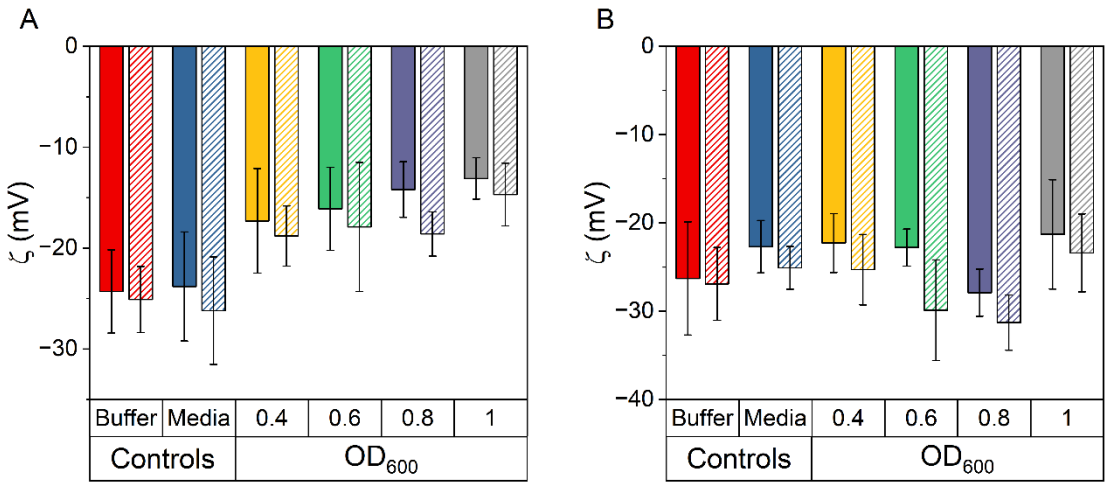


**Figure A3.** Zeta potential of 40 nm AgNPs before and after 2 hr incubations with **(A)** asynchronous *C. crescentus* SM and **(B)** synchronous *C. crescentus* SM**.**

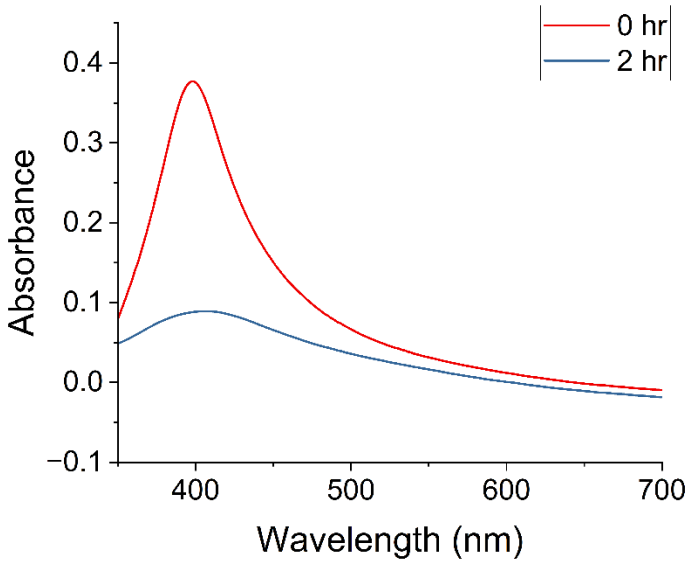


**Figure A4.** Representative UV-Vis spectra of AgNPs taken upon addition of C. crescentus SM and after 2 hours of incubation.

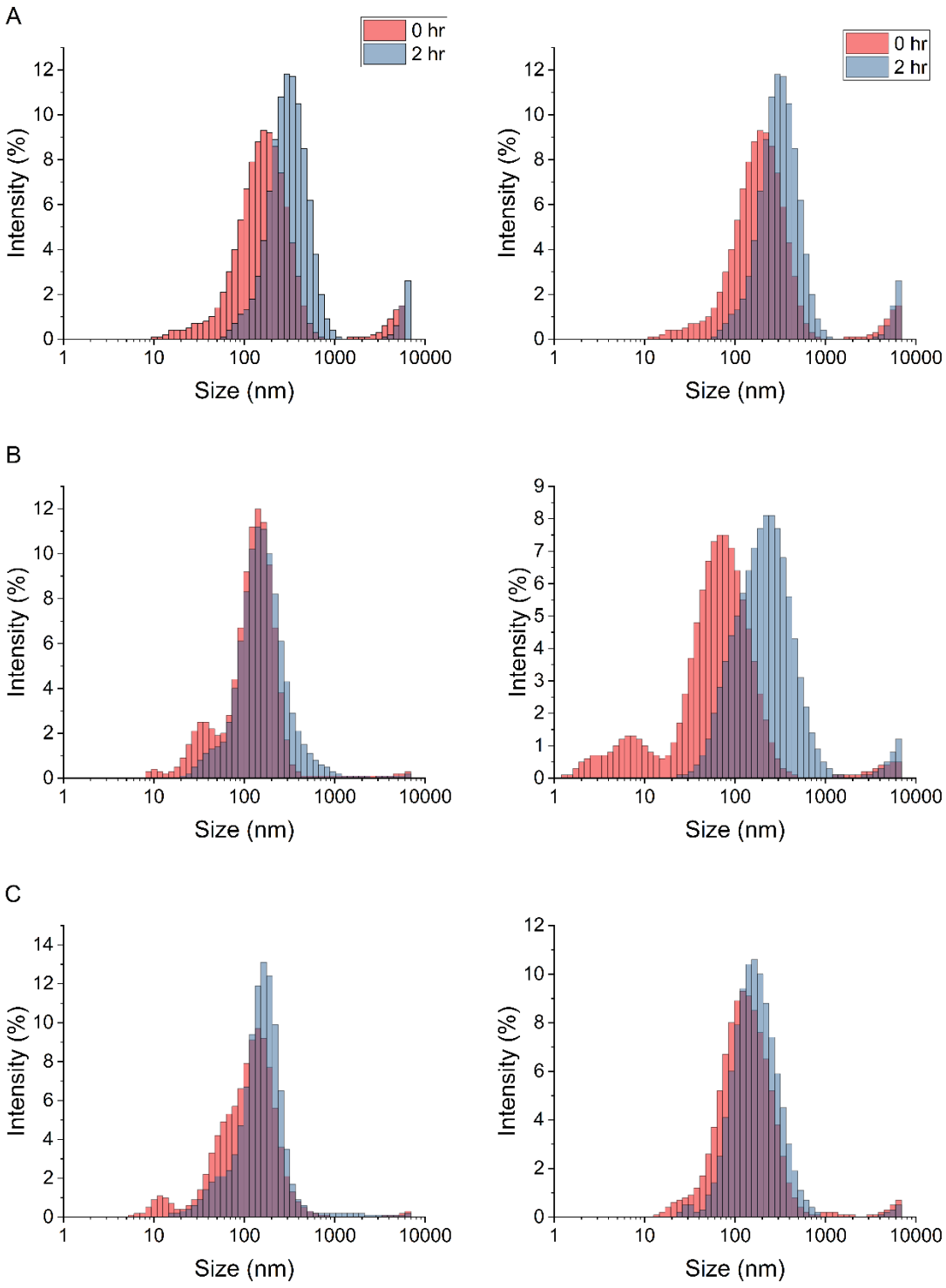


**Figure A5.** DLS histograms showing the averaged size distributions of synchronous (left) and asynchronous (right) of 10 nm AgNPs before and after incubation with **(A)** buffer, **(B)** media, and **(C)** 0.4 OD SM**.**

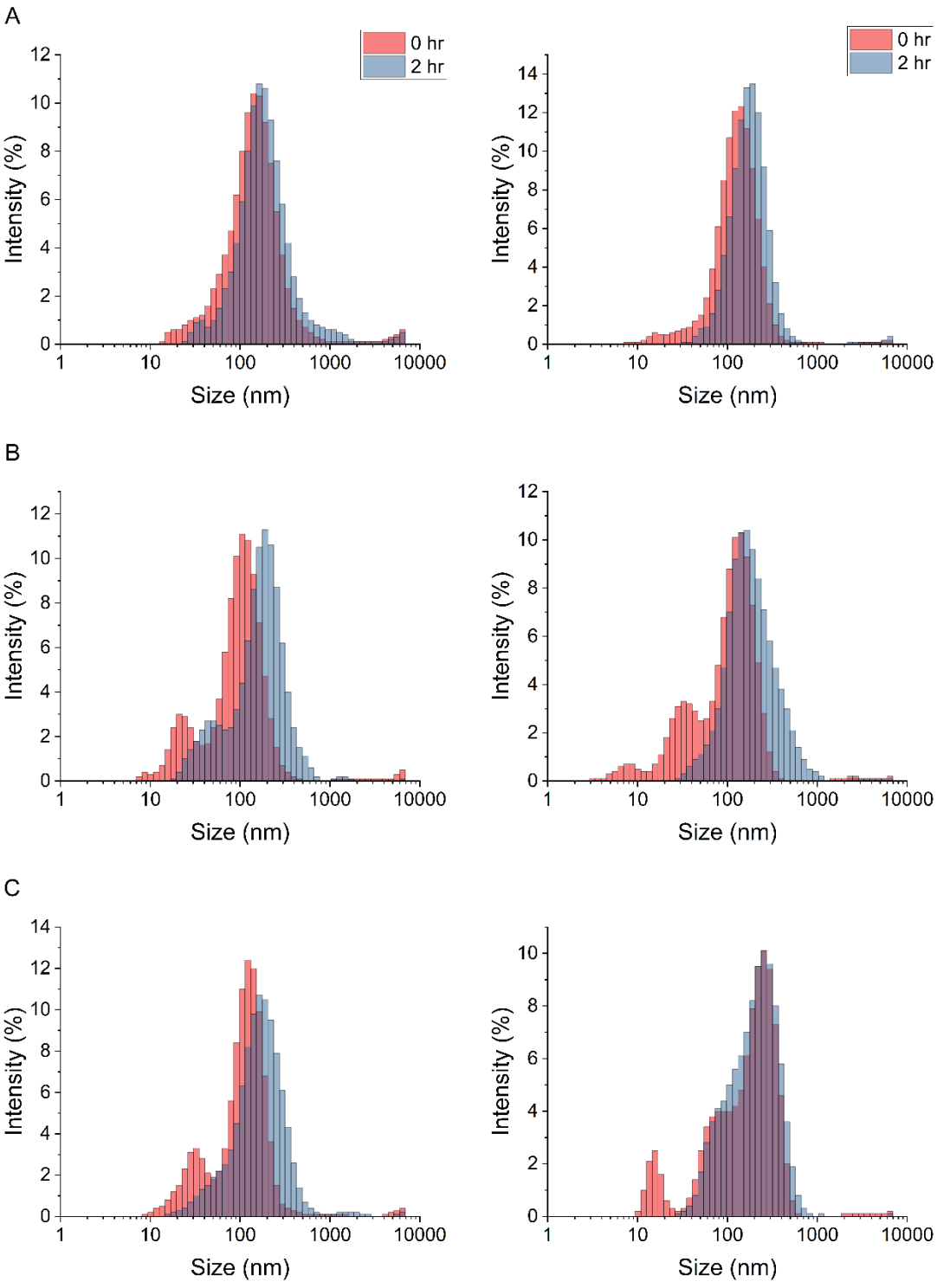


**Figure A6.** DLS histograms showing the averaged size distributions of synchronous (left) and asynchronous (right) of 10 nm AgNPs before and after incubation with **(A)** 0.6 OD SM, **(B)** 0.8 OD SM, and **(C)** 1.0 OD SM.

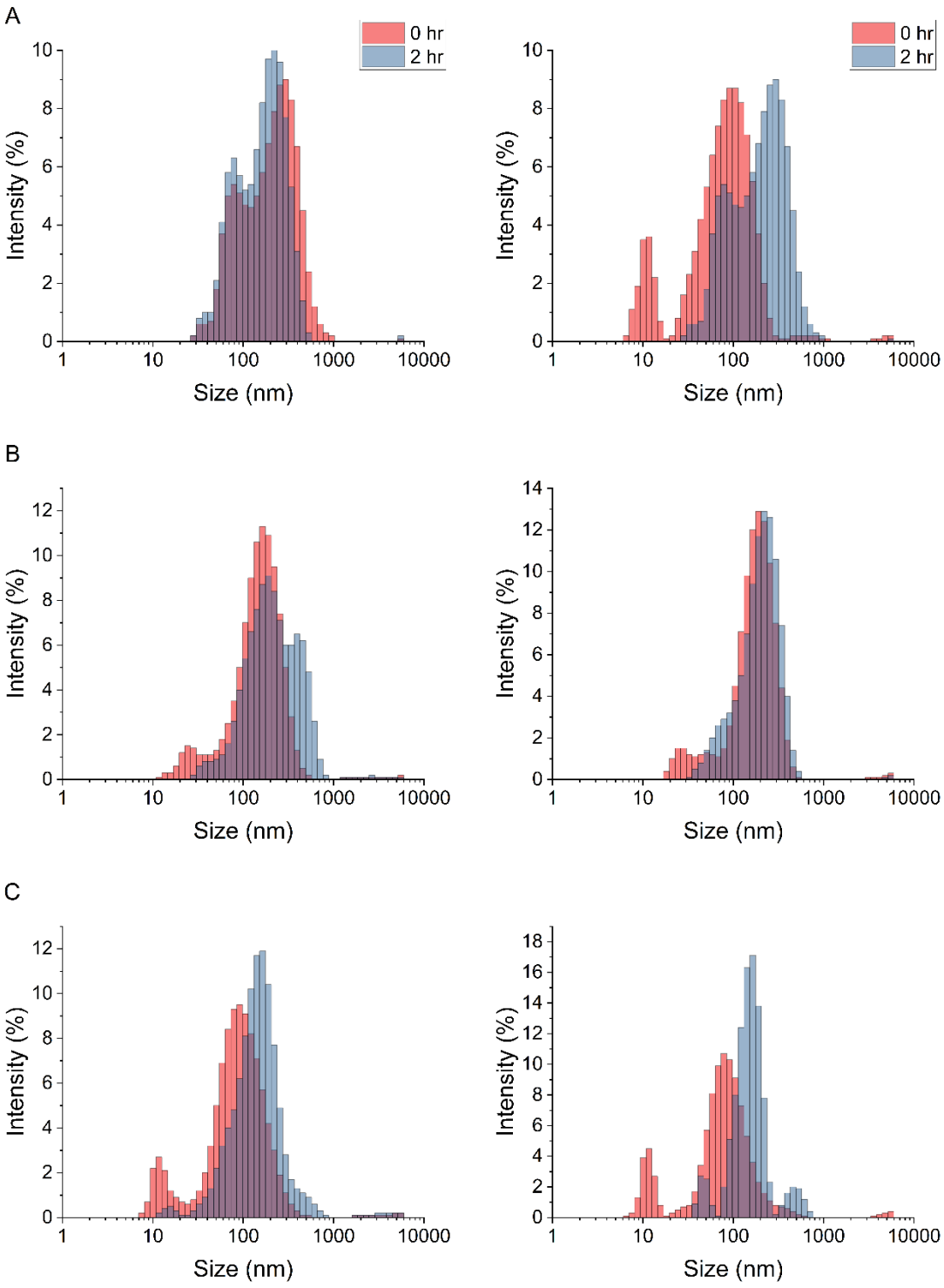


**Figure A7.** DLS histograms showing the averaged size distributions of synchronous (left) and asynchronous (right) of 40 nm AgNPs before and after incubation with **(A)** buffer, **(B)** media, and **(C)** 0.4 OD SM.

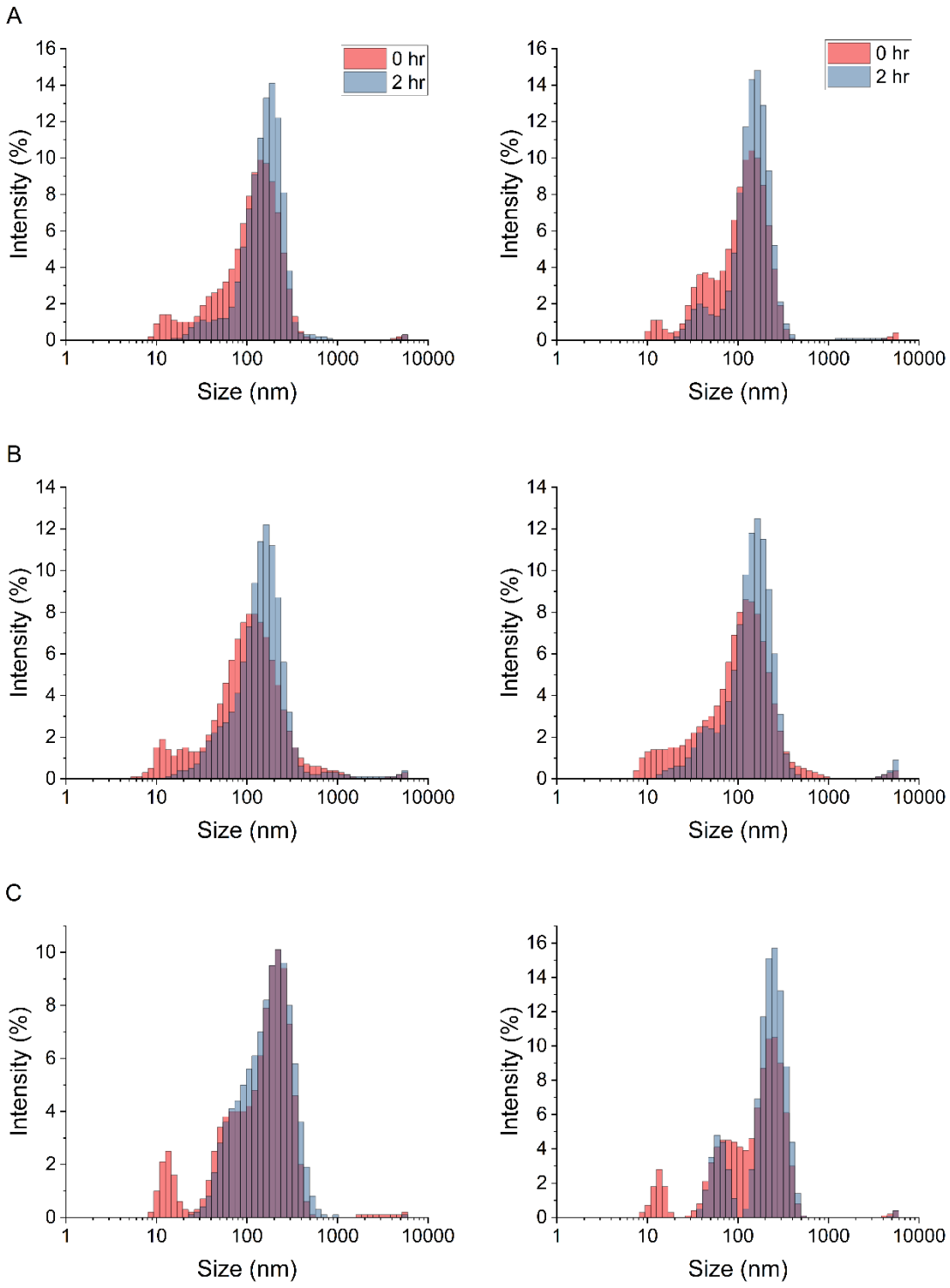


**Figure A8.** DLS histograms showing the averaged size distributions of synchronous (left) and asynchronous (right) of 40 nm AgNPs before and after incubation with **(A)** 0.6 OD SM, **(B)** 0.8 OD SM, and **(C)** 1.0 OD SM.

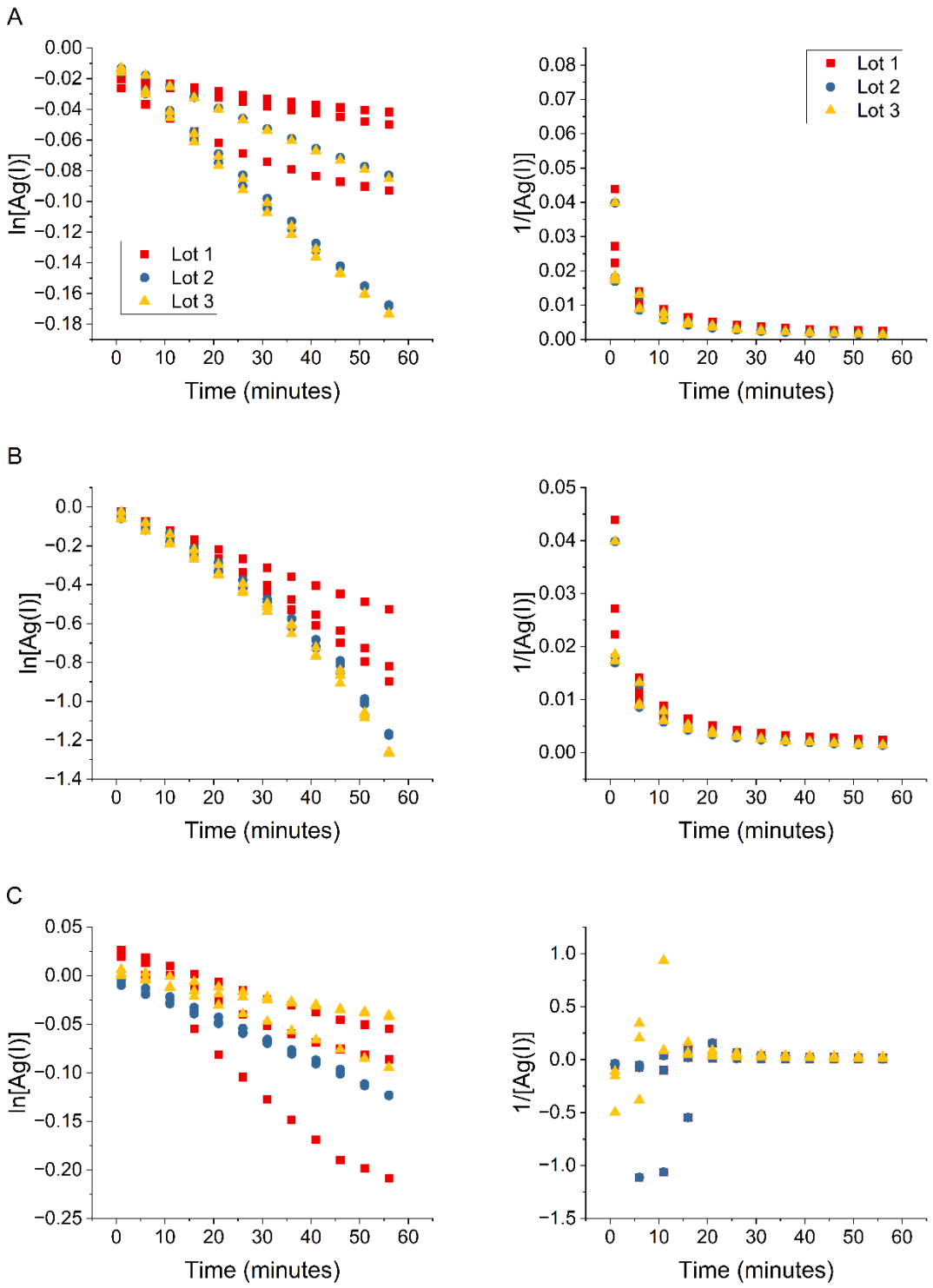


**Figure A9.** First and second order kinetic fits for LSSV data of 10 nm AgNPs in **(A)** buffer, **(B)** M2G media, and **(C)** synchronous 0.4 OD SM. All first order data was fit to a linear model with $R^2 > 0.95$.

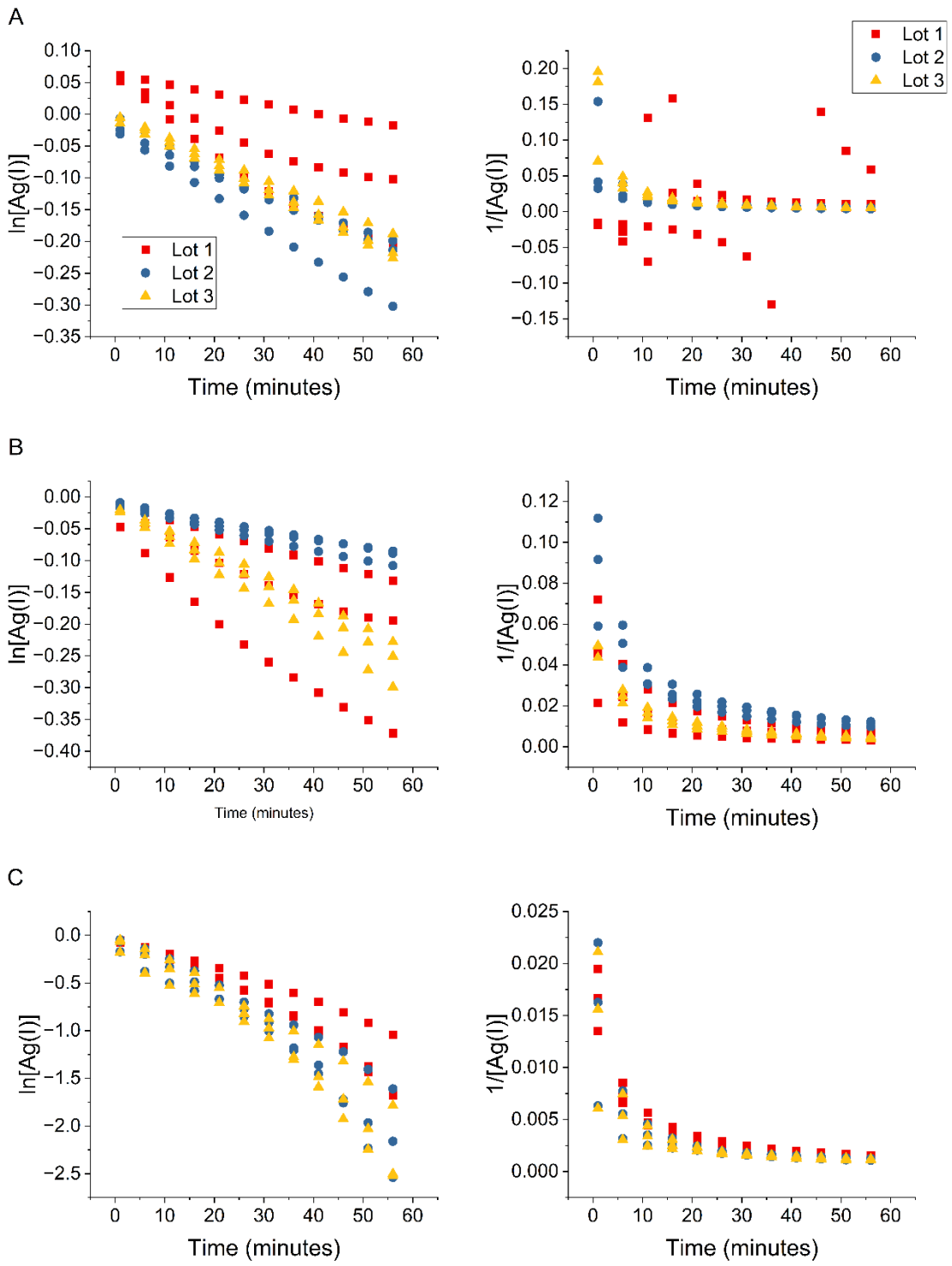


**Figure A10.** First and second order kinetic fits for LSSV data of 10 nm AgNPs in synchronous **(A)** 0.6 OD SM, **(B)** 0.8 OD SM, and **(C)** 1.0 OD SM. All first order data was fit to a linear model with $R^2 > 0.95$.

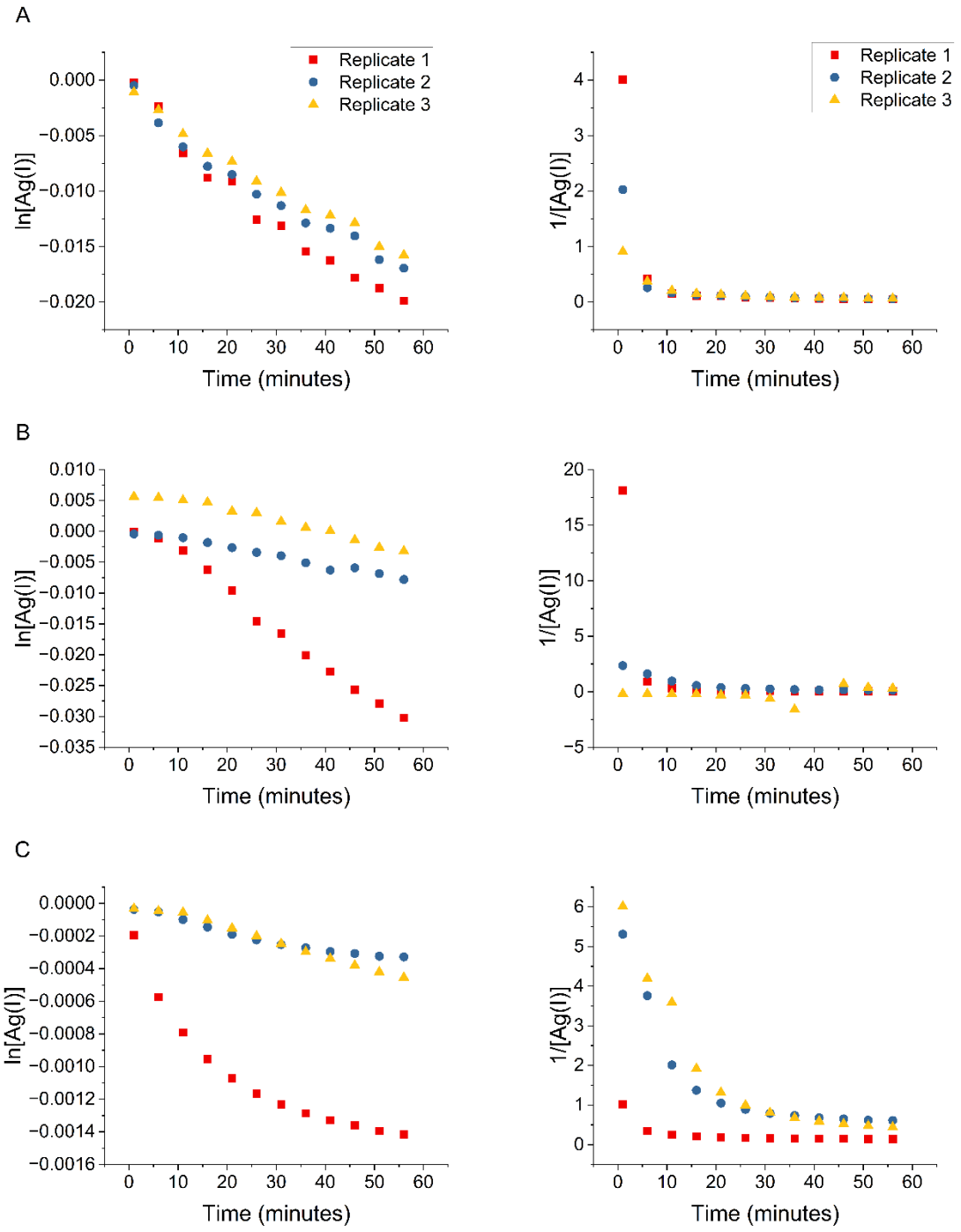


**Figure A11.** First and second order kinetic fits for LSSV data of 40 nm AgNPs in **(A)** buffer, **(B)** M2G media, and **(C)** synchronous 0.4 OD SM. All first order data was fit to a linear model with $R^2 > 0.95$.

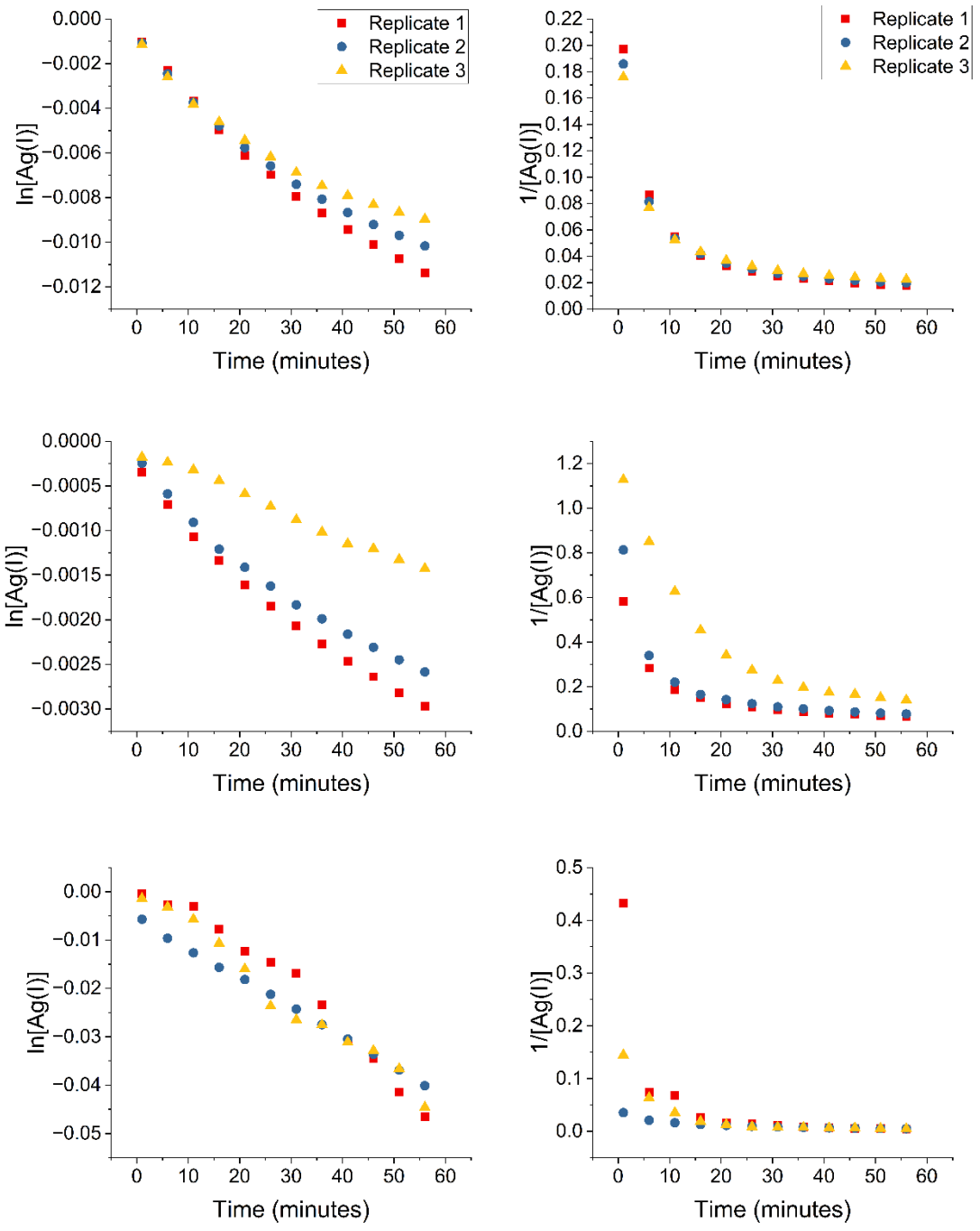


**Figure A12.** First and second order kinetic fits for LSSV data of 10 nm AgNPs in synchronous **(A)** 0.6 OD SM, **(B)** 0.8 OD SM, and **(C)** 1.0 OD SM. All first order data was fit to a linear model with $R^2 > 0.95$.

**Table A1.** Average protein concentrations in asynchronous *C. crescentus* SM obtained through BCA assays (n=3).

| $OD_{600}$ of SM mixture | [Protein] (mg/L) |
|---|---|
| 0.4 | 770 ± 430 |
| 0.6 | 660 ± 390 |
| 0.8 | 670 ± 360 |
| 1.0 | 480 ± 100 |

**Table A2.** Average protein concentrations in synchronous *C. crescentus* SM obtained through BCA assays (n=3).

| $OD_{600}$ of SM mixture | [Protein] (mg/L) |
|---|---|
| 0.4 | 300 ± 20 |
| 0.6 | 450 ± 20 |
| 0.8 | 650 ± 20 |
| 1.0 | 860 ± 20 |

**Table A3.** Hydrodynamic diameters, PDIs, and zeta potentials of asynchronous *C. crescentus* SM obtained through DLS.[a]

| | Condition | $d_H$ (nm) | PDI | ζ (mV) |
|---|---|---|---|---|
| $OD_{600}$ | 0.4 | 790 ± 210 | 0.61 ± 0.20 | -4 ± 1 |
| | 0.6 | 850 ± 120 | 0.61 ± 0.15 | -5 ± 1 |
| | 0.8 | 820 ± 300 | 0.53 ± 0.13 | -6 ± 2 |
| | 1.0 | 1080 ± 440 | 0.41 ± 0.18 | -5 ± 1 |

[a]AgNPs were analyzed at room temperature following initial addition of SM (0 hrs) and after 2 hrs in order to mimic the conditions of later discussed dissolution studies.

**Table A4.** Hydrodynamic diameters, PDIs, and zeta potentials of synchronous *C. crescentus* SM obtained through DLS.[a]

| | Condition | $d_H$ (nm) | PDI | ζ (mV) |
|---|---|---|---|---|
| $OD_{600}$ | 0.4 | 200 ± 50 | 0.34 ± 0.08 | -10 ± 2 |
| | 0.6 | 240 ± 30 | 0.44 ± 0.10 | -15 ± 3 |
| | 0.8 | 270 ± 60 | 0.48± 0.11 | -18 ± 9 |
| | 1.0 | 310 ± 120 | 0.57 ± 0.12 | -24 ± 11 |

[a]AgNPs were analyzed at room temperature following initial addition of SM (0 hrs) and after 2 hrs in order to mimic the conditions of later discussed dissolution studies.

**Table A5.** Hydrodynamic diameters, PDIs, and zeta potentials of 10 nm AgNPs before and after 2-hr incubations with asynchronous *C. crescentus* SM obtained using DLS.[a]

| | Condition | | $d_H$ (nm) | PDI | ζ (mV) |
|---|---|---|---|---|---|
| Controls | Buffer | 0 hrs | 60 ± 10 | 0.48 ± 0.07 | -24 ± 3 |
| | | 2 hrs | 100 ± 10 | 0.41 ± 0.03 | -27 ± 4 |
| | PYE | 0 hrs | 80 ± 10 | 0.51 ± 0.08 | -19 ± 3 |
| | | 2 hrs | 110 ± 10 | 0.50 ± 0.06 | -20 ± 2 |
| $OD_{600}$ | 0.4 | 0 hrs | 90 ± 10 | 0.40 ± 0.02 | -14 ± 2 |
| | | 2 hrs | 130 ± 10 | 0.34 ± 0.03 | -15 ± 1 |
| | 0.6 | 0 hrs | 100 ± 10 | 0.43 ± 0.03 | -16 ± 2 |
| | | 2 hrs | 140 ± 10 | 0.37 ± 0.01 | -20 ± 1 |
| | 0.8 | 0 hrs | 60 ± 10 | 0.47 ± 0.05 | -10 ± 1 |
| | | 2 hrs | 120 ± 10 | 0.49 ± 0.08 | -16 ± 2 |
| | 1.0 | 0 hrs | 70 ± 10 | 0.48 ± 0.05 | -14 ± 2 |
| | | 2 hrs | 120 ± 20 | 0.40 ± 0.04 | -16 ± 1 |

[a]AgNPs were analyzed at room temperature following initial addition of SM (0 hrs) and after 2 hrs in order to mimic the conditions of later discussed dissolution studies.

**Table A6.** Hydrodynamic diameters, PDIs, and zeta potentials of 40 nm AgNPs before and after 2-hr incubations with asynchronous *C. crescentus* SM obtained using DLS.[a]

| | Condition | | $d_H$ (nm) | PDI | ζ (mV) |
|---|---|---|---|---|---|
| Controls | Buffer | 0 hrs | 60 ± 20 | 0.41 ± 0.07 | -24 ± 4 |
| | | 2 hrs | 90 ± 30 | 0.35 ± 0.03 | -25 ± 3 |
| | PYE | 0 hrs | 70 ± 10 | 0.49 ± 0.10 | -24 ± 5 |
| | | 2 hrs | 160 ± 60 | 0.46 ± 0.07 | -26 ± 5 |
| $OD_{600}$ | 0.4 | 0 hrs | 80 ± 20 | 0.45 ± 0.09 | -17 ± 5 |
| | | 2 hrs | 130 ± 20 | 0.43 ± 0.06 | -19 ± 3 |
| | 0.6 | 0 hrs | 100 ± 30 | 0.53 ± 0.13 | -16 ± 4 |
| | | 2 hrs | 160 ± 50 | 0.49 ± 0.08 | -18 ± 6 |
| | 0.8 | 0 hrs | 100 ± 20 | 0.51 ± 0.09 | -14 ± 3 |
| | | 2 hrs | 150 ± 30 | 0.52 ± 0.07 | -19 ± 2 |
| | 1.0 | 0 hrs | 130 ± 50 | 0.39 ± 0.06 | -13 ± 2 |
| | | 2 hrs | 120 ± 20 | 0.36 ± 0.04 | -15 ± 3 |

[a]AgNPs were analyzed at room temperature following initial addition of SM (0 hrs) and after 2 hrs in order to mimic the conditions of later discussed dissolution studies.

**Table A7.** Hydrodynamic diameters, PDIs, and zeta potentials of 10 nm AgNPs before and after 2-hr incubations with synchronous *C. crescentus* SM obtained using DLS.[a]

| | Condition | | $d_H$ (nm) | PDI | ζ (mV) |
|---|---|---|---|---|---|
| Controls | Buffer | 0 hrs | 70 ± 30 | 0.47 ± 0.07 | -27 ± 6 |
| | | 2 hrs | 130 ± 20 | 0.42 ± 0.06 | -30 ± 4 |
| | M2G | 0 hrs | 70 ± 20 | 0.55 ± 0.13 | -25 ± 4 |
| | | 2 hrs | 130 ± 10 | 0.43 ± 0.05 | -29 ± 5 |
| $OD_{600}$ | 0.4 | 0 hrs | 40 ± 10 | 0.58 ± 0.09 | -27 ± 7 |
| | | 2 hrs | 160 ± 10 | 0.39 ± 0.05 | -29 ± 4 |
| | 0.6 | 0 hrs | 60 ± 20 | 0.50 ± 0.08 | -27 ± 3 |
| | | 2 hrs | 180 ± 20 | 0.32 ± 0.09 | -30 ± 3 |
| | 0.8 | 0 hrs | 100 ± 20 | 0.51 ± 0.09 | -24 ± 4 |
| | | 2 hrs | 150 ± 30 | 0.52 ± 0.07 | -32 ± 5 |
| | 1.0 | 0 hrs | 130 ± 50 | 0.39 ± 0.06 | -21 ± 3 |
| | | 2 hrs | 120 ± 20 | 0.36 ± 0.04 | -23 ± 3 |

[a]AgNPs were analyzed at room temperature following initial addition of SM (0 hrs) and after 2 hrs in order to mimic the conditions of later discussed dissolution studies.

**Table A8.** Hydrodynamic diameters, PDIs, and zeta potentials of 40 nm AgNPs before and after 2-hr incubations with synchronous *C. crescentus* SM obtained using DLS.[a]

| | Condition | | $d_H$ (nm) | PDI | ζ (mV) |
|---|---|---|---|---|---|
| Controls | Buffer | 0 hrs | 50 ± 30 | 0.44 ± 0.09 | -26 ± 6 |
| | | 2 hrs | 80 ± 20 | 0.38 ± 0.04 | -27 ± 4 |
| | M2G | 0 hrs | 80 ± 10 | 0.51 ± 0.07 | -23 ± 3 |
| | | 2 hrs | 140 ± 30 | 0.42 ± 0.05 | -25 ± 2 |
| $OD_{600}$ | 0.4 | 0 hrs | 70 ± 30 | 0.39 ± 0.11 | -22 ± 3 |
| | | 2 hrs | 120 ± 30 | 0.32 ± 0.08 | -25 ± 4 |
| | 0.6 | 0 hrs | 90 ± 30 | 0.46 ± 0.05 | -23 ± 2 |
| | | 2 hrs | 140 ± 50 | 0.31 ± 0.04 | -30 ± 5 |
| | 0.8 | 0 hrs | 70 ± 20 | 0.51 ± 0.04 | -21 ± 6 |
| | | 2 hrs | 120 ± 20 | 0.36 ± 0.03 | -23 ± 4 |
| | 1.0 | 0 hrs | 100 ± 40 | 0.53 ± 0.07 | -28 ± 3 |
| | | 2 hrs | 150 ± 30 | 0.36 ± 0.06 | -31 ± 3 |

[a]AgNPs were analyzed at room temperature following initial addition of SM (0 hrs) and after 2 hrs in order to mimic the conditions of later discussed dissolution studies.

**Table A9.** Dissolution rate constants ($\times 10^{-3}$ $min^{-1}$) of 40 nm AgNPs incubated with asynchronous *C. crescentus* SM obtained using LSSV.

| | Condition | Replicate 1 | Replicate 2 | Replicate 3 | Average |
|---|---|---|---|---|---|
| Controls | Buffer | 0.448 ± 0.124 | 0.542 ± 0.046 | 0.376 ± 0.052 | 0.455 ± 0.083 |
| | PYE | 0.376 ± 0.052 | 0.478 ± 0.026 | 0.697 ± 0.296 | 0.517 ± 0.164 |
| $OD_{600}$ | 0.4 | 0.905 ± 0.186 | 0.212 ± 0.187 | 0.311 ± 0.029 | 0.476 ± 0.375 |
| | 0.6 | 0.466 ± 0.104 | 0.222 ± 0.099 | 0.870 ± 0.114 | 0.519 ± 0.327 |
| | 0.8 | 0.372 ± 0.131 | 0.446 ± 0.142 | 1.090 ± 0.402 | 0.636 ± 0.395 |
| | 1.0 | 0.672 ± 0.151 | 0.404 ± 0.070 | 0.598 ± 0.049 | 0.558 ± 0.139 |

**Table A10. Dissolution rate constants ($\times 10^{-3}$ $min^{-1}$) of 40 nm AgNPs incubated with synchronous *C. crescentus* SM obtained using LSSV.**

| | Condition | Replicate 1 |
|---|---|---|
| Controls | Buffer | 0.011 ± 0.007 |
| | M2G | 0.055 ± 0.036 |
| $OD_{600}$ | 0.4 | 0.161 ± 0.025 |
| | 0.6 | 0.302 ± 0.025 |
| | 0.8 | 0.587 ± 0.012 |
| | 1.0 | 0.948 ± 0.125 |

**Table A11. Dissolution rate constants ($\times 10^{-3}$ $min^{-1}$) of 10 nm AgNPs incubated with synchronous *C. crescentus* SM obtained using LSSV.**

| | Condition | Replicate 1 | Replicate 2 | Replicate 3 | Average |
|---|---|---|---|---|---|
| Controls | Buffer | 0.727 ± 0.407 | 1.217 ± 0.242 | 0.852 ± 0.119 | 0.932 ± 0.255 |
| | M2G | 1.533 ± 0.511 | 1.456 ± 0.291 | 1.348 ± 0.621 | 1.446 ± 0.093 |
| $OD_{600}$ | 0.4 | 2.657 ± 0.983 | 2.712 ± 0.783 | 2.136 ± 0.564 | 2.501 ± 0.318 |
| | 0.6 | 3.081 ± 0.977 | 3.936 ± 0.883 | 3.686 ± 0.311 | 3.568 ± 0.440 |
| | 0.8 | 4.278 ± 1.021 | 5.335 ± 1.111 | 4.760 ± 0.925 | 4.791 ± 0.529 |
| | 1.0 | 24.461 ± 5.852 | 27.316 ± 3.852 | 21.279 ± 4.961 | 24.352 ± 3.020 |

## References


(1) Palani, G.; Trilaksana, H.; Sujatha, R. M.; Kannan, K.; Rajendran, S.; Korniejenko, K.; Nykiel, M.; Uthayakumar, M. Silver Nanoparticles for Waste Water Management. *Molecules* **2023**, *28* (8), 3520. https://doi.org/10.3390/molecules28083520.

(2) Bruna, T.; Maldonado-Bravo, F.; Jara, P.; Caro, N. Silver Nanoparticles and Their Antibacterial Applications. *Int. J. Mol. Sci.* **2021**, *22* (13), 7202. https://doi.org/10.3390/ijms22137202.

(3) Kokura, S.; Handa, O.; Takagi, T.; Ishikawa, T.; Naito, Y.; Yoshikawa, T. Silver Nanoparticles as a Safe Preservative for Use in Cosmetics. *Nanomedicine Nanotechnol. Biol. Med.* **2010**, *6* (4), 570–574. https://doi.org/10.1016/j.nano.2009.12.002.

(4) Yin, I. X.; Zhang, J.; Zhao, I. S.; Mei, M. L.; Li, Q.; Chu, C. H. The Antibacterial Mechanism of Silver Nanoparticles and Its Application in Dentistry. *Int. J. Nanomedicine* **2020**, *Volume 15*, 2555–2562. https://doi.org/10.2147/IJN.S246764.

(5) Louie, S. M.; Ma, R.; Lowry, G. V. Transformations of Nanomaterials in the Environment. In *Frontiers of Nanoscience*; Elsevier, 2014; Vol. 7, pp 55–87. https://doi.org/10.1016/B978-0-08-099408-6.00002-5.

(6) Hotze, E. M.; Phenrat, T.; Lowry, G. V. Nanoparticle Aggregation: Challenges to Understanding Transport and Reactivity in the Environment. *J. Environ. Qual.* **2010**, *39* (6), 1909–1924. https://doi.org/10.2134/jeq2009.0462.

(7) Flores-López, L. Z.; Espinoza-Gómez, H.; Somanathan, R. Silver Nanoparticles: Electron Transfer, Reactive Oxygen Species, Oxidative Stress, Beneficial and Toxicological Effects. Mini Review. *J. Appl. Toxicol.* **2019**, *39* (1), 16–26. https://doi.org/10.1002/jat.3654.

(8) Ezra, L.; O'Dell, Z. J.; Hui, J.; Riley, K. R. Emerging Investigator Series: Quantifying Silver Nanoparticle Aggregation Kinetics in Real-Time Using Particle Impact Voltammetry Coupled with UV-Vis Spectroscopy. *Environ. Sci. Nano* **2020**, *7* (9), 2509–2521. https://doi.org/10.1039/D0EN00490A.

(9) MacRae, J. D.; Smit, J. Characterization of Caulobacters Isolated from Wastewater Treatment Systems. *Appl. Environ. Microbiol.* **1991**, *57* (3), 751–758. https://doi.org/10.1128/aem.57.3.751-758.1991.

(10) Wheeler, K. E.; Chetwynd, A. J.; Fahy, K. M.; Hong, B. S.; Tochihuitl, J. A.; Foster, L. A.; Lynch, I. Environmental Dimensions of the Protein Corona. *Nat. Nanotechnol.* **2021**, *16* (6), 617–629. https://doi.org/10.1038/s41565-021-00924-1.

(11) Ke, P. C.; Lin, S.; Parak, W. J.; Davis, T. P.; Caruso, F. A Decade of the Protein Corona. *ACS Nano* **2017**, *11* (12), 11773–11776. https://doi.org/10.1021/acsnano.7b08008.

(12) García-Álvarez, R.; Vallet-Regí, M. Hard and Soft Protein Corona of Nanomaterials: Analysis and Relevance. *Nanomater. Basel Switz.* **2021**, *11* (4), 888. https://doi.org/10.3390/nano11040888.

(13) Govers, S. K.; Jacobs-Wagner, C. Caulobacter Crescentus: Model System Extraordinaire. *Curr. Biol.* **2020**, *30* (19), R1151–R1158. https://doi.org/10.1016/j.cub.2020.07.033.

(14) Ambruso, K.; Park, H.-Y.; Riley, K. R. Analysis of the Active Ingredients in Sunscreen: A Multiweek Experiment for the Analytical Chemistry Laboratory. *J. Chem. Educ.* **2023**, *100* (12), 4845–4852. https://doi.org/10.1021/acs.jchemed.3c00808.

(15) Albalawi, F.; Hussein, M. Z.; Fakurazi, S.; Masarudin, M. J. Engineered Nanomaterials: The Challenges and Opportunities for Nanomedicines. *Int. J. Nanomedicine* **2021**, *Volume 16*, 161–184. https://doi.org/10.2147/IJN.S288236.

(16) Montes-Hernandez, G.; Di Girolamo, M.; Sarret, G.; Bureau, S.; Fernandez-Martinez, A.; Lelong, C.; Eymard Vernain, E. In Situ Formation of Silver Nanoparticles (Ag-NPs) onto Textile Fibers. *ACS Omega* **2021**, *6* (2), 1316–1327. https://doi.org/10.1021/acsomega.0c04814.
(17) Calderón-Jiménez, B.; Johnson, M. E.; Montoro Bustos, A. R.; Murphy, K. E.; Winchester, M. R.; Vega Baudrit, J. R. Silver Nanoparticles: Technological Advances, Societal Impacts, and Metrological Challenges. *Front. Chem.* **2017**, *5*. https://doi.org/10.3389/fchem.2017.00006.
(18) Zhang, Q.; Hu, Y.; Masterson, C. M.; Jang, W.; Xiao, Z.; Bohloul, A.; Garcia-Rojas, D.; Puppala, H. L.; Bennett, G.; Colvin, V. L. When Function Is Biological: Discerning How Silver Nanoparticle Structure Dictates Antimicrobial Activity. *iScience* **2022**, *25* (7), 104475. https://doi.org/10.1016/j.isci.2022.104475.
(19) Batley, G. E.; Kirby, J. K.; McLaughlin, M. J. Fate and Risks of Nanomaterials in Aquatic and Terrestrial Environments. *Acc. Chem. Res.* **2013**, *46* (3), 854–862. https://doi.org/10.1021/ar2003368.
(20) Dale, A. L.; Casman, E. A.; Lowry, G. V.; Lead, J. R.; Viparelli, E.; Baalousha, M. Modeling Nanomaterial Environmental Fate in Aquatic Systems. *Environ. Sci. Technol.* **2015**, *49* (5), 2587–2593. https://doi.org/10.1021/es505076w.
(21) Zachariah, Z.; Heuberger, M. P.; Espinosa-Marzal, R. M. Colloidal Interactions—DLVO Theory and Beyond. In *ACS Symposium Series*; Nagarajan, R., Ed.; American Chemical Society: Washington, DC, 2023; Vol. 1457, pp 31–47. https://doi.org/10.1021/bk-2023-1457.ch002.
(22) Hoek, E. M. V.; Agarwal, G. K. Extended DLVO Interactions between Spherical Particles and Rough Surfaces. *J. Colloid Interface Sci.* **2006**, *298* (1), 50–58. https://doi.org/10.1016/j.jcis.2005.12.031.
(23) Zhang, W. Nanoparticle Aggregation: Principles and Modeling. In *Nanomaterial*; Capco, D. G., Chen, Y., Eds.; Advances in Experimental Medicine and Biology; Springer Netherlands: Dordrecht, 2014; Vol. 811, pp 19–43. https://doi.org/10.1007/978-94-017-8739-0_2.
(24) Peretyazhko, T. S.; Zhang, Q.; Colvin, V. L. Size-Controlled Dissolution of Silver Nanoparticles at Neutral and Acidic pH Conditions: Kinetics and Size Changes. *Environ. Sci. Technol.* **2014**, *48* (20), 11954–11961. https://doi.org/10.1021/es5023202.
(25) Molleman, B.; Hiemstra, T. Time, pH, and Size Dependency of Silver Nanoparticle Dissolution: The Road to Equilibrium. *Environ. Sci. Nano* **2017**, *4* (6), 1314–1327. https://doi.org/10.1039/C6EN00564K.
(26) Martin, M. N.; Allen, A. J.; MacCuspie, R. I.; Hackley, V. A. Dissolution, Agglomerate Morphology, and Stability Limits of Protein-Coated Silver Nanoparticles. *Langmuir* **2014**, *30* (38), 11442–11452. https://doi.org/10.1021/la502973z.
(27) Stebounova, L. V.; Guio, E.; Grassian, V. H. Silver Nanoparticles in Simulated Biological Media: A Study of Aggregation, Sedimentation, and Dissolution. *J. Nanoparticle Res.* **2011**, *13* (1), 233–244. https://doi.org/10.1007/s11051-010-0022-3.
(28) Deng, Y.; Sun; Wang; Sui; She; Zhai; Wang. Effect of Particle Size on Solubility, Dissolution Rate, and Oral Bioavailability: Evaluation Using Coenzyme Q10 as Naked Nanocrystals. *Int. J. Nanomedicine* **2012**, 5733. https://doi.org/10.2147/IJN.S34365.

(29) Cornelis, G.; DooletteMadeleine Thomas, C.; McLaughlin, M. J.; Kirby, J. K.; Beak, D. G.; Chittleborough, D. Retention and Dissolution of Engineered Silver Nanoparticles in Natural Soils. *Soil Sci. Soc. Am. J.* **2012**, *76* (3), 891–902. https://doi.org/10.2136/sssaj2011.0360.
(30) McShan, D.; Ray, P. C.; Yu, H. Molecular Toxicity Mechanism of Nanosilver. *J. Food Drug Anal.* **2014**, *22* (1), 116–127. https://doi.org/10.1016/j.jfda.2014.01.010.
(31) Hwang, E. T.; Lee, J. H.; Chae, Y. J.; Kim, Y. S.; Kim, B. C.; Sang, B.; Gu, M. B. Analysis of the Toxic Mode of Action of Silver Nanoparticles Using Stress-Specific Bioluminescent Bacteria. *Small* **2008**, *4* (6), 746–750. https://doi.org/10.1002/smll.200700954.
(32) Choi, O.; Deng, K. K.; Kim, N.-J.; Ross, L.; Surampalli, R. Y.; Hu, Z. The Inhibitory Effects of Silver Nanoparticles, Silver Ions, and Silver Chloride Colloids on Microbial Growth. *Water Res.* **2008**, *42* (12), 3066–3074. https://doi.org/10.1016/j.watres.2008.02.021.
(33) Lee, B.; Lee, M. J.; Yun, S. J.; Kim, K.; Choi, I.-H.; Park, S. Silver Nanoparticles Induce Reactive Oxygen Species-Mediated Cell Cycle Delay and Synergistic Cytotoxicity with 3-Bromopyruvate in Candida Albicans, but Not in Saccharomyces Cerevisiae. *Int. J. Nanomedicine* **2019**, *Volume 14*, 4801–4816. https://doi.org/10.2147/IJN.S205736.
(34) Navya, P. N.; Daima, H. K. Rational Engineering of Physicochemical Properties of Nanomaterials for Biomedical Applications with Nanotoxicological Perspectives. *Nano Converg.* **2016**, *3* (1), 1. https://doi.org/10.1186/s40580-016-0064-z.
(35) Mahmoudi, M.; Landry, M. P.; Moore, A.; Coreas, R. The Protein Corona from Nanomedicine to Environmental Science. *Nat. Rev. Mater.* **2023**, *8* (7), 422–438. https://doi.org/10.1038/s41578-023-00552-2.
(36) Simonson, T.; Brooks, C. L. Charge Screening and the Dielectric Constant of Proteins: Insights from Molecular Dynamics. *J. Am. Chem. Soc.* **1996**, *118* (35), 8452–8458. https://doi.org/10.1021/ja960884f.
(37) Nienhaus, K.; Nienhaus, G. U. Mechanistic Understanding of Protein Corona Formation around Nanoparticles: Old Puzzles and New Insights. *Small* **2023**, *19* (28), 2301663. https://doi.org/10.1002/smll.202301663.
(38) Jung, S.-Y.; Lim, S.-M.; Albertorio, F.; Kim, G.; Gurau, M. C.; Yang, R. D.; Holden, M. A.; Cremer, P. S. The Vroman Effect: A Molecular Level Description of Fibrinogen Displacement. *J. Am. Chem. Soc.* **2003**, *125* (42), 12782–12786. https://doi.org/10.1021/ja037263o.
(39) Noh, H.; Vogler, E. A. Volumetric Interpretation of Protein Adsorption: Competition from Mixtures and the Vroman Effect. *Biomaterials* **2007**, *28* (3), 405–422. https://doi.org/10.1016/j.biomaterials.2006.09.006.
(40) Cai, R.; Ren, J.; Guo, M.; Wei, T.; Liu, Y.; Xie, C.; Zhang, P.; Guo, Z.; Chetwynd, A. J.; Ke, P. C.; Lynch, I.; Chen, C. Dynamic Intracellular Exchange of Nanomaterials' Protein Corona Perturbs Proteostasis and Remodels Cell Metabolism. *Proc. Natl. Acad. Sci.* **2022**, *119* (23), e2200363119. https://doi.org/10.1073/pnas.2200363119.
(41) Mu, Q.; Jiang, G.; Chen, L.; Zhou, H.; Fourches, D.; Tropsha, A.; Yan, B. Chemical Basis of Interactions Between Engineered Nanoparticles and Biological Systems. *Chem. Rev.* **2014**, *114* (15), 7740–7781. https://doi.org/10.1021/cr400295a.
(42) Gunsolus, I. L.; Mousavi, M. P. S.; Hussein, K.; Bühlmann, P.; Haynes, C. L. Effects of Humic and Fulvic Acids on Silver Nanoparticle Stability, Dissolution, and Toxicity. *Environ. Sci. Technol.* **2015**, *49* (13), 8078–8086. https://doi.org/10.1021/acs.est.5b01496.

(43) Wang, X.; Fan, W.; Dong, Z.; Liang, D.; Zhou, T. Interactions of Natural Organic Matter on the Surface of PVP-Capped Silver Nanoparticle under Different Aqueous Environment. *Water Res.* **2018**, *138*, 224–233. https://doi.org/10.1016/j.watres.2018.03.048.
(44) Brown, J.; Shannahan, J.; Podila, R. A Hyperspectral and Toxicological Analysis of Protein Corona Impact on Silver Nanoparticle Properties, Intracellular Modifications, and Macrophage Activation. *Int. J. Nanomedicine* **2015**, 6509. https://doi.org/10.2147/IJN.S92570.
(45) Aizawa, S.-I. Caulobacter Crescentus — Alteration between Flagellum and Stalk. In *The Flagellar World*; Elsevier, 2014; pp 32–33. https://doi.org/10.1016/B978-0-12-417234-0.00008-6.
(46) Haiko, J.; Westerlund-Wikström, B. The Role of the Bacterial Flagellum in Adhesion and Virulence. *Biology* **2013**, *2* (4), 1242–1267. https://doi.org/10.3390/biology2041242.
(47) Lasker, K.; Mann, T. H.; Shapiro, L. An Intracellular Compass Spatially Coordinates Cell Cycle Modules in Caulobacter Crescentus. *Curr. Opin. Microbiol.* **2016**, *33*, 131–139. https://doi.org/10.1016/j.mib.2016.06.007.
(48) Nyarko, A.; Barton, H.; Dhinojwala, A. Investigating the Material Properties of the Caulobacter Crescentus Adhesive Holdfast. *Biophys. J.* **2016**, *110* (3), 467a. https://doi.org/10.1016/j.bpj.2015.11.2503.
(49) Vestby, L. K.; Grønseth, T.; Simm, R.; Nesse, L. L. Bacterial Biofilm and Its Role in the Pathogenesis of Disease. *Antibiotics* **2020**, *9* (2), 59. https://doi.org/10.3390/antibiotics9020059.
(50) Donlan, R. M. Biofilms: Microbial Life on Surfaces. *Emerg. Infect. Dis.* **2002**, *8* (9), 881–890. https://doi.org/10.3201/eid0809.020063.
(51) Collier, J. Cell Division Control in Caulobacter Crescentus. *Biochim. Biophys. Acta BBA - Gene Regul. Mech.* **2019**, *1862* (7), 685–690. https://doi.org/10.1016/j.bbagrm.2018.04.005.
(52) Brown, P. J. B.; Hardy, G. G.; Trimble, M. J.; Brun, Y. V. Complex Regulatory Pathways Coordinate Cell-Cycle Progression and Development in Caulobacter Crescentus. In *Advances in Microbial Physiology*; Elsevier, 2008; Vol. 54, pp 1–101. https://doi.org/10.1016/S0065-2911(08)00001-5.
(53) Hartl, J.; Kiefer, P.; Kaczmarczyk, A.; Mittelviefhaus, M.; Meyer, F.; Vonderach, T.; Hattendorf, B.; Jenal, U.; Vorholt, J. A. Untargeted Metabolomics Links Glutathione to Bacterial Cell Cycle Progression. *Nat. Metab.* **2020**, *2* (2), 153–166. https://doi.org/10.1038/s42255-019-0166-0.
(54) Kawano, Y.; Suzuki, K.; Ohtsu, I. Current Understanding of Sulfur Assimilation Metabolism to Biosynthesize L-Cysteine and Recent Progress of Its Fermentative Overproduction in Microorganisms. *Appl. Microbiol. Biotechnol.* **2018**, *102* (19), 8203–8211. https://doi.org/10.1007/s00253-018-9246-4.
(55) Hottes, A. K.; Meewan, M.; Yang, D.; Arana, N.; Romero, P.; McAdams, H. H.; Stephens, C. Transcriptional Profiling of *Caulobacter Crescentus* during Growth on Complex and Minimal Media. *J. Bacteriol.* **2004**, *186* (5), 1448–1461. https://doi.org/10.1128/JB.186.5.1448-1461.2004.
(56) Stephens, C.; Christen, B.; Fuchs, T.; Sundaram, V.; Watanabe, K.; Jenal, U. Genetic Analysis of a Novel Pathway for D -Xylose Metabolism in *Caulobacter Crescentus*. *J. Bacteriol.* **2007**, *189* (5), 2181–2185. https://doi.org/10.1128/JB.01438-06.

(57) Parveen, N.; Cornell, K. A. Methylthioadenosine/S-adenosylhomocysteine Nucleosidase, a Critical Enzyme for Bacterial Metabolism. *Mol. Microbiol.* **2011**, *79* (1), 7–20. https://doi.org/10.1111/j.1365-2958.2010.07455.x.
(58) Christen, M.; Kulasekara, H. D.; Christen, B.; Kulasekara, B. R.; Hoffman, L. R.; Miller, S. I. Asymmetrical Distribution of the Second Messenger C-Di-GMP upon Bacterial Cell Division. *Science* **2010**, *328* (5983), 1295–1297. https://doi.org/10.1126/science.1188658.
(59) Abel, S.; Bucher, T.; Nicollier, M.; Hug, I.; Kaever, V.; Abel Zur Wiesch, P.; Jenal, U. Bi-Modal Distribution of the Second Messenger c-Di-GMP Controls Cell Fate and Asymmetry during the Caulobacter Cell Cycle. *PLoS Genet.* **2013**, *9* (9), e1003744. https://doi.org/10.1371/journal.pgen.1003744.
(60) Kaczmarczyk, A.; Hempel, A. M.; Von Arx, C.; Böhm, R.; Dubey, B. N.; Nesper, J.; Schirmer, T.; Hiller, S.; Jenal, U. Precise Timing of Transcription by C-Di-GMP Coordinates Cell Cycle and Morphogenesis in Caulobacter. *Nat. Commun.* **2020**, *11* (1), 816. https://doi.org/10.1038/s41467-020-14585-6.
(61) Jung, A.; Eisheuer, S.; Cserti, E.; Leicht, O.; Strobel, W.; Möll, A.; Schlimpert, S.; Kühn, J.; Thanbichler, M. Molecular Toolbox for Genetic Manipulation of the Stalked Budding Bacterium Hyphomonas Neptunium. *Appl. Environ. Microbiol.* **2015**, *81* (2), 736–744. https://doi.org/10.1128/AEM.03104-14.
(62) Chertkov, O.; Brown, P. J. B.; Kysela, D. T.; De Pedro, M. A.; Lucas, S.; Copeland, A.; Lapidus, A.; Del Rio, T. G.; Tice, H.; Bruce, D.; Goodwin, L.; Pitluck, S.; Detter, J. C.; Han, C.; Larimer, F.; Chang, Y.; Jeffries, C. D.; Land, M.; Hauser, L.; Kyrpides, N. C.; Ivanova, N.; Ovchinnikova, G.; Tindall, B. J.; Göker, M.; Klenk, H.-P.; Brun, Y. V. Complete Genome Sequence of Hirschia Baltica Type Strain (IFAM 1418T). *Stand. Genomic Sci.* **2011**, *5* (3), 287–297. https://doi.org/10.4056/sigs.2205004.
(63) Dutta, A.; Smith, B.; Goldman, T.; Walker, L.; Streets, M.; Eden, B.; Dirmeier, R.; Bowman, J. S. Understanding Microbial Community Dynamics in Up-Flow Bioreactors to Improve Mitigation Strategies for Oil Souring. *Front. Microbiol.* **2020**, *11*, 585943. https://doi.org/10.3389/fmicb.2020.585943.
(64) Hui, J.; O'Dell, Z. J.; Rao, A.; Riley, K. R. In Situ Quantification of Silver Nanoparticle Dissolution Kinetics in Simulated Sweat Using Linear Sweep Stripping Voltammetry. *Environ. Sci. Technol.* **2019**, *53* (22), 13117–13125. https://doi.org/10.1021/acs.est.9b04151.
(65) Bhattacharjee, S. DLS and Zeta Potential – What They Are and What They Are Not? *J. Controlled Release* **2016**, *235*, 337–351. https://doi.org/10.1016/j.jconrel.2016.06.017.
(66) Tomaszewska, E.; Soliwoda, K.; Kadziola, K.; Tkacz-Szczesna, B.; Celichowski, G.; Cichomski, M.; Szmaja, W.; Grobelny, J. Detection Limits of DLS and UV-Vis Spectroscopy in Characterization of Polydisperse Nanoparticles Colloids. *J. Nanomater.* **2013**, *2013*, 1–10. https://doi.org/10.1155/2013/313081.
(67) Thomas, E. M.; Testa, S. M. The Colorimetric Determination of Selectively Cleaved Adenosines and Guanosines in DNA Oligomers Using Bicinchoninic Acid and Copper. *JBIC J. Biol. Inorg. Chem.* **2017**, *22* (1), 31–46. https://doi.org/10.1007/s00775-016-1405-4.
(68) Herr, K. L.; Carey, A. M.; Heckman, T. I.; Chávez, J. L.; Johnson, C. N.; Harvey, E.; Gamroth, W. A.; Wulfing, B. S.; Van Kessel, R. A.; Marks, M. E. Exopolysaccharide Production in Caulobacter Crescentus: A Resource Allocation Trade-off between Protection

and Proliferation. *PLOS ONE* **2018**, *13* (1), e0190371.
https://doi.org/10.1371/journal.pone.0190371.